Chemical Engineering & Processing: Process Intensification 143 (2019) 107602

Contents lists available at ScienceDirect

Chemical Engineering & Processing: Process Intensification

journal homepage: www.elsevier.com/locate/cep

On the influences of surface heat release and thermal radiation upon transport in catalytic porous microreactors—A novel porous-solid interface model

Ali Saeed[a], Nader Karimi[a,*], Graeme Hunt[a], Mohsen Torabi[b]

[a] School of Engineering, University of Glasgow, Glasgow, G12 8QQ, United Kingdom
[b] Independent Researcher, Greater Chicago Area, IL 60067, USA

ARTICLE INFO

Keywords:
Exothermic catalytic reactions
Soret effect
Local thermal non-equilibrium
Thermal radiation
Microreactor
Casson fluid

ABSTRACT

A novel porous-solid interface model is put forward to analyse the distribution of heat generated by exothermic catalytic reactions on the inner walls of a porous microreactor. This builds upon a recent theoretical development on the local thermal non-equilibrium interface modelling and further advances that to include thermal radiation. The model is then utilised by an analytical investigation of transport phenomena in a parallel-plates, porous microreactor. Two-dimensional, closed form solutions are developed for the velocity, temperature and concentration fields and analytical expressions are derived for Nusselt and Sherwood number as well as local and total entropy generation. The results show that exothermic catalytic activities can significantly affect the transport processes in microreactor by modifying the values of Nusselt and Sherwood number. This can be highly intensified by an imbalance in the catalytic activities of microreactor surfaces. It is further shown that interactions of the surface heat release with thermal radiation and heat losses through the walls introduce a wealth of Nusselt and Sherwood number behaviours, which considerably differ from those of non-catalytic systems. These clearly demonstrate the importance of including surface heat release in non-equilibrium analyses of the catalytic porous microreactors in which catalysts are placed on the walls.

1. Introduction

Micro-reaction technology offers a promising means of production of decentralised renewable fuels [1,2]. A wide variety of biological feedstocks in the form of liquid and slurry could be reformed and converted to a range of gaseous and liquid fuels through using microreactors [3–5]. Exothermic catalytic reactions are central to micro fuel-processing and often dominate the performance and cost of microreactors [6,7]. Such reactions are heavily influenced by the transport of heat and mass and therefore a precise prediction of transport processes is essential for the design and optimisation of micro fuel processors [1,2]. This, in turn, calls for modelling of heat release on the surface of catalyst, which in microreactors can take place on the internal surface of a microchannel [8,9]. Further, insertion of porous materials in microchannels is a common method of enhancing heat transfer in microreactors accommodating highly exothermic reactions [10–13]. Hence, the analysis of transport phenomena in such porous catalytic microreactors includes heat release on the internal surface of a microchannel filled by a porous medium. This introduces a very rich and challenging modelling problem, which has just started to be explored [14].

Most recently, magnetic fields have been applied to fuel reformers [15,16] with a special emphasis on the magnetic micro-processing of various biofuels for diesel engine applications [17]. Further, it has been recently shown that application of a magnetic field to porous catalytic beds can significantly improve the selectivity of hydrogeneration of CO_2 in methanol production [18,19]. A common feature of reforming and hydrogenation reactions is their temperature sensitivity. This adds a new dimension to the problem of modelling of transfer processes as an imposed magnetic field can affect those through its influences on the fluid flow in microreactor [20]. More importantly, it is now well demonstrated that accurate modelling of transport in catalytic porous microchannels with internal heat generations is subject to consideration of several effects. These include local thermal non-equilibrium (LTNE) [21,22] and thermal radiation in the porous medium [23] and, thermal diffusion of mass in the fluid phase [24,25].

Conventionally, catalytic porous microreactors are modelled numerically or analytically by assuming local thermal equilibrium (LTE),

* Corresponding author.
E-mail address: Nader.Karimi@glasgow.ac.uk (N. Karimi).

https://doi.org/10.1016/j.cep.2019.107602
Received 23 June 2019; Received in revised form 9 July 2019; Accepted 14 July 2019
Available online 29 July 2019
0255-2701/ © 2019 The Authors. Published by Elsevier B.V. This is an open access article under the CC BY license (http://creativecommons.org/licenses/BY/4.0/).

Nomenclature

a_{sf}	Interfacial area per unit volume of porous media (m^{-1})
B_o	Magnetic field intensity (kg/A·s^2)
Bi	Biot Number
Br	Brinkman Number (Modified)
C	Mass species concentration (kg/m^3)
C_0	Inlet Concentration (kg/m^3)
$C_{p,f}$	Specific heat capacity (J/K·kg)
D	Effective mass diffusion coefficient (m^2/s)
Da	Darcy Number
Dn	Damköhler Number
D_T	Coefficient of thermal mass diffusion (kg/K·m·s)
h_1	Half-thickness of the microchannel (m)
h_2	Half-height of the microchannel (m)
h_{sf}	Interstitial heat transfer coefficient (W/K·m^2)
H_w	Wall heat transfer coefficient (W/K·m^2)
k	Effective thermal conductivity ratio of the fluid and the porous solid
k_1	Thermal conductivity of the wall (W/K·m)
k_{e1}	Ratio of thermal conductivity of wall 1 and the thermal conductivity of the wall
k_{e2}	Ratio of thermal conductivity of wall 2 and the thermal conductivity of the wall
k_{ef}	Effective thermal conductivity of the fluid phase (W/K·m)
k_{es}	Effective thermal conductivity of the solid phase of the porous medium (W/K·m)
k_r	Reaction rate constant (kg/m^2·s)
k^*	Absorption coefficient (m^{-1})
L	Length of the microchannel (m)
M	Viscosity Ratio
M_d	Magnetic interaction parameter (modified Hartmann number)
N_{DI}	Dimensionless diffusive irreversibility
N_{FF}	Dimensionless fluid friction irreversibility
N_f	Dimensionless fluid and interstitial (interphase) irreversibility
$N_{f,ht}$	Dimensionless fluid heat transfer irreversibility
N_{int}	Dimensionless interstitial (interphase) heat transfer irreversibility
N_{mg}	Dimensionless magnetic field heat generation irreversibility
N_s	Dimensionless porous solid and interstitial (interphase) irreversibility
$N_{s,ht}$	Dimensionless porous solid heat transfer irreversibility
N_{w1}	Dimensionless wall 1 heat transfer irreversibility
N_{w2}	Dimensionless wall 2 heat transfer irreversibility
N_{pm}	Dimensionless total porous medium irreversibility
N_{Tot}	Dimensionless total entropy irreversibility
Nu	Nusselt Number
p	Pressure (Pa)
Pe	Peclet Number
Pr	Prandtl Number
Q	Wall heat flux ratio
q_{c1}	Total heat flux generated by the lower wall catalyst (W/m^2)
q_{c2}	Total heat flux generated by the upper wall catalyst (W/m^2)
q_{w1}	Lower wall heat flux (W/m^2)
q_{w2}	Upper wall heat flux (W/m^2)
q_1	Lower channel porous media heat flux (W/m^2)
q_2	Upper channel porous media heat flux (W/m^2)
Re	Reynolds Number
R	Specific gas Constant (J/K·kg)
S	Shape factor of the porous medium
S_f	Volumetric Source term (W/m^3)
$S_{DI}^{'''}$	Volumetric entropy generation due to mass diffusion (W/K·m^3)
$S_{FF}^{'''}$	Volumetric entropy generation due to fluid friction (W/K·m^3)
$S_f^{'''}$	Volumetric entropy generation in the fluid (W/K·m^3)
$S_s^{'''}$	Volumetric entropy generation in the porous solid (W/K·m^3)
Sr	Soret Number
T	Temperature (K)
u	Fluid velocity (m/s)
U	Dimensionless fluid velocity (m/s)
$\bar{u}$	Average fluid velocity (m/s)
$\bar{U}$	Dimensionless average fluid velocity (m/s)
x	Axial coordinate
X	Dimensionless axial coordinate
y	Transverse coordinate
Y	Dimensionless transverse coordinate

Greek Symbols

μ	Dynamic viscosity (kg/m·s)
κ	Permeability (m^2)
ρ	Density (kg/m^3)
θ	Dimensionless temperature
Φ	Dimensionless concentration
ξ	Aspect ratio of microchannel
ε	Porosity of the porous medium
γ	Magnetic Angle (Radians)
ω	Dimensionless heat flux
ω_f	Dimensionless volumetric source term
φ	Irreversibility distribution ratio
β	Casson fluid parameter
σ	Electrical Conductivity (A^2·s^3/kg·m^2)
σ^*	Stefan-Boltzmann constant (W/m^2·K^4)

Subscripts

s	Porous Solid
f	Casson Fluid
1	Lower
2	Upper
w	Wall

see for example Refs. [26,27]. This modelling approach ignores the local temperature differences between the solid and fluid phases in the porous medium and treats the medium as a homogenous mixture of solid and fluid phases [28]. Catalytic heat release is then modelled as a simple surface heat release in a channel filled with an effective fluid. A great mathematical convenience is therefore offered with the cost of jeopardizing the accuracy of calculations under certain conditions. Over the last a few years, a number of studies have shown that porous channels and microchannels featuring internal heat release can significantly deviate from LTE, e.g. [21,22,25]. Hence, implementation of LTNE is a necessity in the analysis of transport phenomena in microreactors with exothermic catalytic reactions. Two energy equations coupled with the internal heat exchanges between the solid and fluid phases of the porous medium are employed in LTNE approach [28]. This requires utilisation of the so-called 'porous-solid interface model', which describes the distribution of a surface heat flux between the solid

and fluid phases of the porous medium on its interfaces with a solid wall [29].

Although in general LTNE is a well-developed technique, a major difficulty arises when the interface between a solid wall and a porous medium involves heat release by surface reactions. This is because the produced heat on the interface can take three different routes including the solid wall of the microreactor as well as the solid and fluid phases of the porous medium. However, currently all established porous-solid interface models ignore heat conduction in the solid wall by assuming the wall thickness to be negligibly small [28,30,31]. Yet, such assumption is highly dubious in microreactors as there exist significant evidence about the influences of wall thickness on the thermal performance of microreactors and microchannels [6,32]. Most recently, this issue was resolved theoretically by Hunt et al. [14] through extending an existing porous-solid interface model to include the wall effects. These authors showed that their extended interface model could be successfully implemented in the thermal analysis of catalytic microreactors with exothermic surface reactions [14]. It should be emphasised that porous-solid interface models are central to all theoretical and numerical LTNE analyses of porous channels and microchannels, see for example [33–35]. Hence, advancement in interface modelling is key to improving the analysis of transport phenomena in a wide range of applications.

Although the mathematical validity of the interface model of Hunt et al. [14] was rigorously demonstrated, the influences of added complexities remain to be further explored. Since the chemistry of exothermic catalytic reactions is often heavily temperature dependent, an accurate modelling of heat transport processes around the catalyst is of paramount importance. In a magnetic biofuel micro-reformer, this requires a rather complex multiphysics analysis that considers the magnetohydrodynamics (MHD) and all thermal effects. Despite its practical relevance, to the best of authors' knowledge, so far, little attention has been paid to this problem. Therefore, the aim of the current work is to put forward a robust analytical methodology for such analysis with an emphasis on the theoretical modelling of catalytic heat release on a porous-solid interface. This builds upon the recent theoretical developments by Hunt et al. [14] and extends that to include thermal radiation as well as non-Newtonian fluid and magnetic effects. A two-dimensional heat and mass transfer analysis complimented by that of entropy generation is also reported to further investigate the effects of pertinent physicochemical processes.

2. Theoretical methods

2.1. Problem configuration and assumptions

Fig. 1 shows a schematic view of the investigated parallel-plate catalytic porous microreactor. This includes a thick-wall microchannel fully-filled by a porous material. The outer most surfaces of the microchannel is subject to constant but unequal heat fluxes and the catalyst is placed on the inner surfaces of the walls. This configuration is the essential building block of real microreactors consisting of a bundle of microchannels [6]. A uniform flow of an electrically conductive Casson fluid enters the system from the left-hand side (see Fig. 1). Casson fluid has been chosen as a fair representation of the non-Newtonian characteristics of the biofuels in magnetic fuel reforming [17]. In general, Casson fluid rheology is described by [36,37]

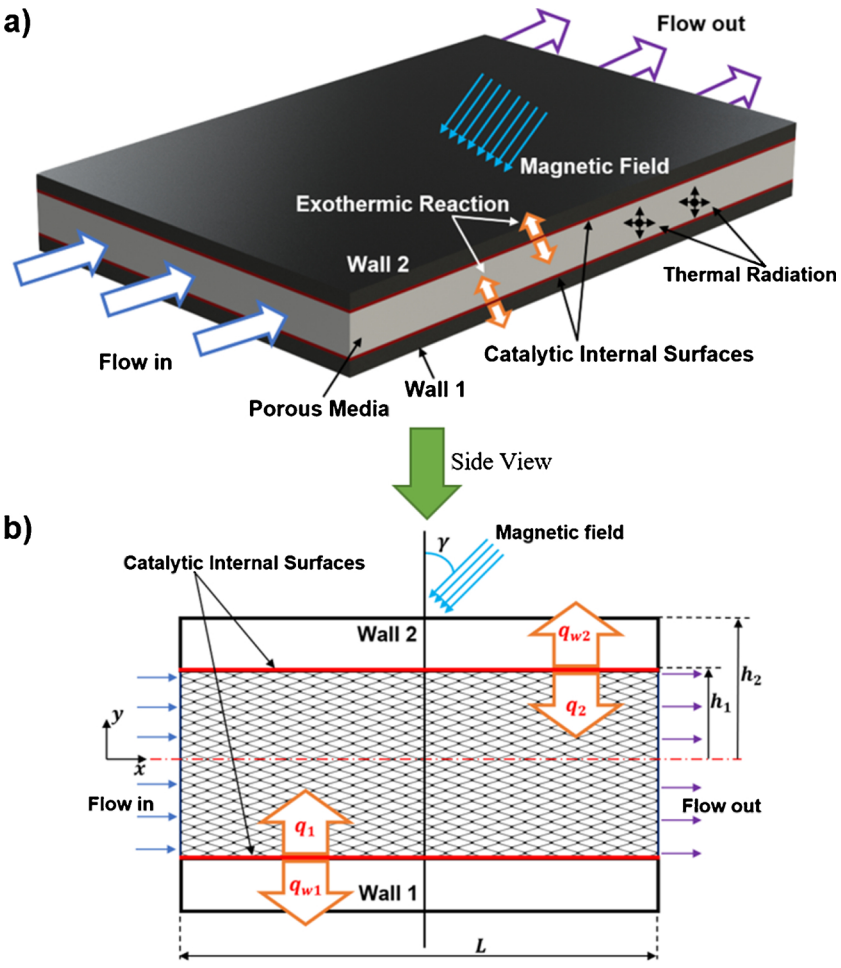

Fig. 1. Isometric (a) and schematic side view (b) of the porous microchannel under investigation.

$$\tau_{ij} = \begin{cases} 2\left(\mu_b + \frac{p_y}{\sqrt{2\pi}}\right)e_{ij} & \pi > \pi_c \\ 2\left(\mu_b + \frac{p_y}{\sqrt{2\pi c}}\right)e_{ij} & \pi < \pi_c \end{cases} \quad (1)$$

In Eq. (1), τ_{ij} is the (i, j)-th component of the stress tensor, $\pi_{ij} = e_{ij}e_{ij}$ and e_{ij} are the (i, j)-th component of the deformation rate. The parameter π is the product of the component of deformation rate with itself, π_c represents a critical value of this product based on the non-Newtonian model. Further, μ_b and p_y denote the plastic dynamic viscosity and the yield stress of the considered fluid. The kinematic viscosity suitable for Casson fluid is often given by $\vartheta_f = \frac{\mu_b}{\rho}(1 + \beta)$ [36].

It is emphasised that the non-Newtonian Casson fluid is not a central element of the proceeding analyses and has been considered solely for representation of biofuel flows. The following assumptions are further made in the rest of this work.

- The parallel-plate catalytic microreactor is axisymmetric geometrically but asymmetric to catalytic heat release. It is also subject to uneven wall heat fluxes and a uniform magnetic field, which can change with an adjustable angle with respect to the axis of the microreactor.
- The flow of Casson fluid is steady and fully developed.
- The porous medium is homogenous and under LTNE condition.
- A zeroth order, temperature independent, exothermic surface reaction occurs on the catalyst coated of the internal surfaces of the top and bottom plates, examples of such configuration can be found in Refs. [38–40].
- The thermal diffusion of mass through Soret effect is considered.
- Gravitational effects are ignored but thermal radiation throughout the porous medium is considered.
- Axial heat transfer in the solid walls of the microreactor are ignored [6].

A question may arise about the practicality of an asymmetric microreactor in the real world. In response, it is noted that although the use of two different catalytic layers in one microchannel is unlikely, the magnetic field can render one catalytic layer more active [41]. This is particularly the case when the magnetic field makes an arbitrary orientation with the plane of the flow and thus can make the flow inside the microchannel three-dimensional. Such complex fluid mechanics are not modelled here. Nevertheless, the net effect on the catalyst will be enhancement or suppression of the catalytic activity and hence altering the heat release. Another reason could be unequal poisoning of the catalytic surfaces, which makes their activities different.

2.2. Governing equations and boundary conditions

Transport of momentum in the porous microchannel in the presence of MHD and non-Newtonian effects are described by [20,42,43]

$$-\frac{\partial p}{\partial x} + \mu_{eff}\left(1 + \frac{1}{\beta}\right)\frac{\partial^2 u}{\partial y^2} - \frac{\mu_f\left(1 + \frac{1}{\beta}\right)}{\kappa}u \quad -h_1 \le y < h_1$$
$$-\sigma B_o^2 u \sin^2(\gamma) = 0. \quad (2)$$

In Eq. (2), the first three terms on the left-hand side are those of classical Darcy-Brinkman model with viscosity modifications for the considered Casson fluid [42,43] and the last term represents the MHD induced force [20]. The transport of thermal energy in the walls as well as in the fluid and solid phases of the porous section of the microreactor are given by the following set of equations. It is emphasised that the transport equations in the porous microchannel are two-dimensional and include the axial variation of temperature in addition to its transversal changes [23,44].

$$k_2\frac{\partial}{\partial y}\left[\frac{\partial T_2}{\partial y}\right] = 0 \quad h_1 < y \le h_2 \quad (3a)$$

$$k_{ef}\frac{\partial^2 T_f}{\partial y^2} + h_{sf}a_{sf}(T_s - T_f) + \sigma B_o^2(u\sin^2(\gamma))^2 \quad -h_1 \le y < h_1$$
$$= \rho_f C_{p,f} u\frac{\partial T_f}{\partial x} \quad (3b)$$

$$k_{es}\frac{\partial^2 T_s}{\partial y^2} - h_{sf}a_{sf}(T_s - T_f) - \left(\frac{\partial q}{\partial y}\right) = 0 \quad -h_1 \le y < h_1 \quad (3c)$$

$$k_1\frac{\partial}{\partial y}\left[\frac{\partial T_1}{\partial y}\right] = 0 \quad -h_2 < y \le -h_1 \quad (3d)$$

The thermal radiation term in Eq. (3c) is given by the following expression [45,46]

$$q = -\frac{4\sigma^*}{3k^*}\frac{\partial T_s^4}{\partial y}. \quad (4)$$

Rosseland approximation [23,47] is then used to further simplify Eq. (4) and convert it to the following relation.

$$\frac{\partial q}{\partial y} = \frac{-16\sigma^* T_o^3}{3k^*}\frac{\partial^2 T_s}{\partial y^2}. \quad (5)$$

The boundary conditions associated with Eqs. (3a-d) are respectively expressed by the following set of relations.

y value Boundary Conditions

$$h_2 \quad k_2\frac{\partial T_2}{\partial y}\bigg|_{y=h_2} = -q_{w2} \quad (6a)$$

$$h_1 \quad u_f = 0,\ T_f = T_s = T_2,\ q_{c2} = k_{ef}\frac{\partial T_f}{\partial y}\bigg|_{y=h_1} + \left(k_{es} + \frac{16\sigma^* T_o^3}{3k^*}\right)\frac{\partial T_s}{\partial y}\bigg|_{y=h_1}$$
$$- k_2\frac{\partial T_2}{\partial y}\bigg|_{y=h_1} \quad (6b)$$

$$-h_1 \quad u_f = 0,\ T_f = T_s = T_1,\ q_{c1} = -k_{ef}\frac{\partial T_f}{\partial y}\bigg|_{y=-h_1}$$
$$-\left(k_{es} + \frac{16\sigma^* T_o^3}{3k^*}\right)\frac{\partial T_s}{\partial y}\bigg|_{y=-h_1} + k_1\frac{\partial T_1}{\partial y}\bigg|_{y=-h_1} \quad (6c)$$

$$-h_2 \quad k_1\frac{\partial T_1}{\partial y}\bigg|_{y=-h_2} = q_{w1} \quad (6d)$$

It is important to note that Eq. (6c) is the modified version of the porous-solid interface model recently developed by Hunt et al. [14]. The interface model of Hunt considers diffusion of the heat of catalytic reactions into the solid wall and porous solid [14]. Yet, it ignores the thermal radiation from the porous solid. Equation (6c) advances this model by adding the thermal radiation to the diffusion term of the porous solid phase.

The two-dimensional transport of species within the fluid phase is expressed by the following two-dimensional advective-diffusive model, in which the Soret effect is also included [44,48,49]

$$u\frac{\partial C}{\partial x} = D\frac{\partial^2 C}{\partial^2 y} - D_T\frac{\partial^2 T_f}{\partial y^2} \quad -h_1 \le y < h_1 \quad (7)$$

Given the zeroth order catalytic reaction on the internal surface of the walls and the asymmetricity of the problem, the boundary conditions of Eq. (7) are expressed by the followings [44].

$$x = 0,\ y = -h_1,\ C = C_0 \quad (8a)$$

$$y = 0,\ D\frac{\partial C}{\partial y} = D_T\frac{\partial T_f}{\partial y}. \tag{8b}$$

2.3. Non-dimensionalising and analytical solution

The governing equations and boundary conditions reported in Eqs. (2)–(8) are then non-dimensionalised. Since the current problem includes several physicochemical processes, a relatively large number of dimensionless parameters are needed to non-dimensionalise the equations. These dimensionless parameters are listed in Table 1.

Using the introduced dimensionless parameters, the momentum equation and its boundary conditions reduce to the followings

$$1 + M\left(1 + \frac{1}{\beta}\right)\frac{\partial^2 U}{\partial Y^2} - U\left[\frac{1}{Da}\left(1 + \frac{1}{\beta}\right) + M_d\sin^2(\gamma)\right] - Y_1 \le Y < Y_1 = 0 \tag{9}$$

$$U(Y_1) = U(-Y_1) = 0. \tag{10a,b}$$

Analytical solution of Eq. (9) with incorporation of boundary conditions (10) results in the following velocity profile across the microchannel.

$$U(Y) = \frac{Da}{\left(1 + \frac{1}{\beta}\right) + DaM_d\sin^2(\gamma)}\left[1 - \frac{\cosh(SY)}{\cosh(SY_1)}\right]. \tag{11}$$

The average flow velocity takes the form of

$$\bar{U} = \frac{Da}{\left(1 + \frac{1}{\beta}\right) + DaM_d\sin^2(\gamma)}\left[1 - \frac{\tanh(SY_1)}{SY_1}\right], \tag{12}$$

and the velocity ratios can be written as

$$u/\bar{u} = U/\bar{U} = D_1[\cosh(SY_1) - \cosh(SY)]. \tag{13}$$

The fully developed condition of the flow results in the following relations [33,34]

$$\frac{\partial T_f}{\partial x} = \frac{\partial \bar{T}_f}{\partial x} = \frac{\partial T_s}{\partial x} = \frac{\partial \bar{T}_s}{\partial x} = \frac{\partial T_w}{\partial x} = \Omega = Constant, \tag{14}$$

and thus, the temperature field can be decomposed into an axial and a transversal component as described in the following expression [11,23]

$$T_i(x, y) = T_i(y) + \Omega x,\ i = 1,2,\ s,\ f \tag{15}$$

Considering the thermal boundary condition given by Eq. (6) and integration of the energy equation for the fluid phase reveals

$$q_1 + q_2 + \sigma B_o^2\sin^4(\gamma)\int_{-h_1}^{h_1} u^2 dy = \rho_f C_{p,f}\int_{-h_1}^{h_1} u\frac{\partial T_f}{\partial x}dy, \tag{16}$$

and therefore:

$$\frac{d\bar{T}_f}{dx} = \frac{1}{2\rho_f C_{p,f}\bar{u}h_1}\left[q_1 + q_2 + \frac{2\mu_{eff}M_d}{M}\sin^4(\gamma)D_1^2\bar{u}^{-2}h_2\left(Y_1\cosh^2(SY_1) + \frac{SY_1 - 3\cosh(SY_1)\sinh(SY_1)}{2S}\right)\right], \tag{17}$$

in which the average fluid temperature is defined as

$$\bar{T}_f = \frac{1}{2\bar{u}h_1}\int_{-h_1}^{h_1} uT_f dy. \tag{18}$$

Equations (17) and (18) can be now used to produce the dimensionless form of the energy equations (Eq. 3a-3d), which read

$$k_{e2}\theta_2'' = 0 \quad Y_1 < Y \le 1 \tag{19a}$$

$$k\theta_f'' + Bi[\theta_s - \theta_f] + D_2\cosh(2SY) + D_3\cosh(SY) + D_4 \quad -Y_1 \le Y < Y1 = 0 \tag{19b}$$

$$(1 + R_d)\theta_s'' - Bi[\theta_s - \theta_f] = 0 \quad -Y_1 \le Y < Y1 \tag{19c}$$

$$k_{e1}\theta_1'' = 0 \quad -Y_1 < Y \le -1 \tag{19d}$$

The analytical solutions of Eqs. (19a) and (19d) are straightforward. However, Eqs. (19b) and (19c) need to be decoupled before closed-form solutions can be sought for them. Through conducting an algebraic manipulation explained in the literature [21,22,34], these equations are converted to two fourth-order, decoupled ordinary differential equations that can be readily solved analytically.

$$\theta_f'''' - Q_1\theta_f'' + Q_2\cosh(2SY) + Q_3\cosh(SY) - Q_4 = 0 \tag{20a}$$

Table 1
Dimensionless Parameters.

$Da = \frac{\kappa}{h_2^2}$	$M = \frac{\mu_{eff}}{\mu_f}$	$M_d = \frac{\sigma B_0^2 h_2^2}{\mu_f}$
$\theta_i = \frac{(T_i - T_{w,in})k_{es}}{(q_1+q_2)h_2},\ i = 1,2,s,f$	$S = \sqrt{\frac{\frac{1}{Da}\left(1+\frac{1}{\beta}\right) + M_d\sin^2(\gamma)}{\left(1+\frac{1}{\beta}\right)M}}$	$U = \frac{u}{u_r},\ u_r = -\frac{h_2^2}{\mu_f}\frac{\partial p}{\partial x}$
$Bi = \frac{h_{sf}a_{sf}h_2^2}{k_{es}}$	$Br = \frac{\mu_{eff}\bar{u}^{-2}}{(q_1+q_2)h_2}$	$k_{e1} = \frac{k_1}{k_{es}}$
$k_{e2} = \frac{k_2}{k_{es}}$	$k = \frac{k_{ef}}{k_{es}} = \frac{\varepsilon k_f}{(1-\varepsilon)k_s}$	$R_d = \frac{16\sigma^* T_0^3}{3k^* k_{es}}$
$Q = \frac{q_2}{q_1+q_2}$	$Q_{w1} = \frac{q_{w1}}{q_1+q_2}$	$q_1 = q_{c1} - q_{w1}$
$Q_{w2} = \frac{q_{w2}}{q_1+q_2}$	$q_2 = q_{c2} - q_{w2}$	$Y = \frac{y}{h_2}$
$Y_1 = \frac{h_1}{h_2}$	$X = \frac{x}{L}$	$Re = \frac{2h_2\rho_f\bar{u}^{-2}}{\mu_{eff}}$
$\xi = \frac{h_2}{L}$	$\Pr = \frac{C_{p,f}\mu_{eff}}{k_{ef}}$	$\Phi = \frac{C}{C_0}$
$Dn = \frac{k_r h_1}{DC_0}$	$Pe = \frac{h_1\bar{u}}{D}$	$Sr = \frac{(q_1+q_2)h_1 D_T}{C_0 k_f D}$
$N_i = \frac{S_i''' h_2^2}{k_{es}},\ i = w_1, w_2, s, f,\ FF,\ DI$	$\varphi = \frac{RDC_0}{k_{es}}$	$\omega = \frac{q_1 h_2}{k_{es}T_{w,in}}$

$$\theta_s'''' - Q_1\theta_s'' - [Q_5\cosh(2SY) + Q_6\cosh(SY) + Q_4] = 0 \quad (20b)$$

The dimensionless thermal boundary conditions are expressed by the followings

$$\theta_2(Y_1) = \theta_{w2},\ \theta_2'(1) = -\frac{Q_{w2}}{k_{e2}}, \quad (21a,b)$$

$$\theta_f(Y_1) = \theta_s(Y_1) = \theta_{w2}, \quad (21c,d)$$

$$\theta_f(-Y_1) = \theta_s(-Y_1) = 0, \quad (21e,f)$$

$$\theta_f''(Y_1) = -\frac{1}{k}[D_2\cosh(2SY_1) + D_3\cosh(SY_1) + D_4],\ \theta_s''(Y_1) = 0, \quad (21g,h)$$

$$\theta_f''''(0) = \theta_s''''(0) = 0, \quad (21i,j)$$

$$\theta_1(-Y_1) = 0,\ \theta_1'(-1) = \frac{Q_{w1}}{k_{e1}}. \quad (21k,l)$$

Considering the dimensionless boundary conditions, the closed-form solutions of the transversal temperature distribution are expressed by the followings where the constants E_1 to E_{14} are given in Appendix A.

$$\theta_2(Y) = E_1 + E_2 Y \quad Y_1 < Y \le 1 \quad (22a)$$

$$\theta_f(Y) = E_3\cosh(2SY) + E_4\cosh(SY) + E_5\cosh(\alpha Y) + E_6 Y^2 + E_7 Y + E_8 \quad -Y_1 \le Y < Y1 \quad (22b)$$

$$\theta_s(Y) = E_9\cosh(2SY) + E_{10}\cosh(SY) + E_{11}\cosh(\alpha Y) + E_6 Y^2 + E_7 Y + E_{12} \quad -Y_1 \le Y < Y1 \quad (22c)$$

$$\theta_1(Y) = E_{13} + E_{14} Y \quad -Y_1 < Y \le -1 \quad (22d)$$

$$\alpha = \sqrt{Q_1}. \quad (23)$$

Further, the axial gradient of the temperature can be evaluated as follows

$$\frac{d\bar{\theta}_f}{dX} = \Omega = \frac{1}{k\xi Y_1 PrRe}\left[1 + 2BrD_1^2\frac{M_d}{M}\sin^4(\gamma)\left(Y_1\cosh^2(SY_1) + \frac{SY_1 - 3\cosh(SY_1)\sinh(SY_1)}{2S}\right)\right]. \quad (24)$$

Recalling the decomposition of the temperature field into axial and transversal components (Eq. 15), the dimensionless temperature fields in the solid and fluid phases of the system can be expressed by the following equations.

$$\theta_2(X, Y) = E_1 + E_2 Y + \Omega X \quad Y_1 < Y \le 1 \quad (25a)$$

$$\theta_f(X, Y) = E_3\cosh(2SY) + E_4\cosh(SY) + E_5\cosh(\alpha Y) + E_6 Y^2 + E_7 Y + E_8 + \Omega X \quad -Y_1 \le Y < Y1 \quad (25b)$$

$$\theta_s(X, Y) = E_9\cosh(2SY) + E_{10}\cosh(SY) + E_{11}\cosh(\alpha Y) + E_6 Y^2 + E_7 Y + E_{12} + \Omega X \quad -Y_1 \le Y < Y1 \quad (25c)$$

$$\theta_1(X, Y) = E_{13} + E_{14} Y + \Omega X \quad -Y_1 < Y \le -1 \quad (25d)$$

Similar to the temperature field, the concentration field can be broken into axial and transversal components [21]. That is:

$$C(x, y) = C(y) + C(x). \quad (26)$$

Following the arguments made in Ref. [38], the axial distribution of concentration reduces to

$$\frac{\partial C}{\partial x} = \frac{k_r}{\bar{u}h_1}, \quad (27)$$

and therefore

$$C(x) = \frac{k_r x}{\bar{u}h_1}, \quad (28)$$

which in dimensionless form, is expressed by

$$\Phi(X) = \frac{DnX}{PeY_1\xi}. \quad (29)$$

Thus, the mass transfer equation is converted to the following dimensional and dimensionless forms

$$\frac{uk_r}{\bar{u}h_1} = D\frac{\partial^2 C}{\partial y^2} - D_T\frac{\partial^2 T_f}{\partial y^2}, \quad (30)$$

$$\Phi''(Y) - \left(\frac{U}{\bar{U}}\right)\frac{Dn}{Y_1^2} = \frac{Srk}{\varepsilon Y_1}\theta_f''(Y), \quad (31)$$

with the following dimensionless boundary conditions

$$\Phi(-Y_1) = 1,\ \Phi'(0) = \frac{Srk}{Y_1\varepsilon}\theta_f'(0). \quad (32a,b)$$

Analytical solution of Eq. (31) yields an expression in the form of

$$\Phi(Y) = F_1\cosh(2SY) + F_2\cosh(SY) + F_3\cosh(\alpha Y) + F_4 Y^2 + F_5 Y + F_6, \quad (33)$$

and incorporating the axial part of the solution renders the full analytical solution for the concentration field, while the constants F_1 to F_6 are provided by Appendix A.

$$\Phi(X, Y) = F_1\cosh(2SY) + F_2\cosh(SY) + F_3\cosh(\alpha Y) + F_4 Y^2 + F_5 Y + F_6 + \frac{DnX}{PeY_1\xi} \quad (34)$$

The analytical solutions provided in this section are all in closed form and do not involve any iterative numerical method. To derive the particular solutions of the governing equations, Wolfram Mathematica was used.

2.4. Nusselt and Sherwood number

The convection coefficient for the lower and upper walls of the microchannel is defined by the following relations [50].

$$H_{w1} = \frac{q_1}{T_{w1} - \bar{T}_f}, \quad (35a)$$

$$H_{w2} = \frac{q_2}{T_{w2} - \bar{T}_f}, \quad (35b)$$

Accordingly, the Nusselt number on the internal surface of the top and bottom walls is given by:

$$Nu_{w1} = \frac{2H_{w1}h_1}{k_{ef}} = \frac{2q_1h_1}{k_{ef}(T_{w1} - \bar{T}_f)}, \quad (36a)$$

$$Nu_{w2} = \frac{2H_{w2}h_1}{k_{ef}} = \frac{2q_2h_1}{k_{ef}(T_{w2} - \bar{T}_f)}. \quad (36b)$$

Using the dimensionless parameters, Eq. (36a) and (36b) can be manipulated to yield:

$$Nu_{w1} = \frac{2Y_1(Q-1)}{k\bar{\theta}_f}, \quad (37a)$$

$$Nu_{w2} = \frac{2QY_1}{k(\theta_{w2} - \bar{\theta}_f)}, \quad (37b)$$

in which the dimensionless form of the average temperature is defined as

$$\bar{\theta}_f = \frac{D_1}{2Y_1}\int_{-Y_1}^{Y1} \theta_f(Y)[\cosh(SY_1) - \cosh(SY)]dY. \tag{38}$$

Further, the mass transfer convection coefficient for the current problem can be expressed by [50]

$$H_m = \frac{k_r}{C_0 - \bar{C}}, \tag{39}$$

and the Sherwood number takes the form of

$$Sh = \frac{2H_m h_1}{D} = \frac{2k_r h_1}{D(C_0 - \bar{C})}, \tag{40}$$

where the average concentration is given by the following relation.

$$\bar{C} = \frac{1}{2uh_1}\int_{-h_1}^{h_1} uCdy. \tag{41}$$

Thus, the Sherwood number can be also expressed by the following relations

$$Sh = \frac{2Dn}{(1 - \bar{\Phi})}, \tag{42}$$

$$\bar{\Phi} = \frac{D_1}{2Y_1}\int_{-Y_1}^{Y1} \Phi(Y)[\cosh(SY_1) - \cosh(SY)]dY. \tag{43}$$

2.5. Local and total entropy generation rates

The thermodynamic irreversibilities encountered in the current problem include those due to heat conduction in the solid walls, heat transfer in the solid and fluid phases of the porous medium, fluid friction and mass transfer. These can be represented by the following expressions [51–53]

$$S'''_{w2} = \frac{k_2}{T_2^2}\left[\left(\frac{\partial T_2}{\partial x}\right)^2 + \left(\frac{\partial T_2}{\partial y}\right)^2\right] \tag{44a}$$

$$S'''_{s} = \frac{k_{es}}{T_s^2}\left[\left(\frac{\partial T_s}{\partial x}\right)^2 + \left(\frac{\partial T_s}{\partial y}\right)^2\right] - \frac{h_{sf}a_{sf}(T_s - T_f)}{T_s} \tag{44b}$$

$$S'''_{f} = \frac{k_{ef}}{T_f^2}\left[\left(\frac{\partial T_f}{\partial x}\right)^2 + \left(\frac{\partial T_f}{\partial y}\right)^2\right] + \frac{h_{sf}a_{sf}(T_s - T_f)}{T_f} + \frac{\sigma B_o^2 (usin^2(\gamma))^2}{T_f} \tag{44c}$$

$$S'''_{FF} = \frac{\mu_f\left(1 + \frac{1}{\beta}\right)}{\kappa T_f}u^2 + \frac{\mu_{eff}\left(1 + \frac{1}{\beta}\right)}{T_f}\left(\frac{du}{dy}\right)^2 \tag{44d}$$

$$S'''_{DI} = \frac{RD}{C}\left[\left(\frac{\partial C}{\partial x}\right)^2 + \left(\frac{\partial C}{\partial y}\right)^2\right] + \frac{RD}{T_f}\left[\left(\frac{\partial C}{\partial x}\right)\left(\frac{\partial T_f}{\partial x}\right) + \left(\frac{\partial C}{\partial y}\right)\left(\frac{\partial T_f}{\partial y}\right)\right] \tag{44e}$$

$$S'''_{w1} = \frac{k_1}{T_1^2}\left[\left(\frac{\partial T_1}{\partial x}\right)^2 + \left(\frac{\partial T_1}{\partial y}\right)^2\right] \tag{44f}$$

Non-dimensionalisation of Eqs. (44a-44f) and separation of different sources of irreversibility results in the following expressions (see the nomenclature for definition of each term). These provide a two-dimensional mathematical model of local entropy generation (per unit volume) throughout the microreactor by different sources of irreversibility.

$$N_{w2} = \frac{k_{e2}\omega^2}{(\omega\theta_2 + 1)^2}\left[\xi^2\left(\frac{\partial\theta_2}{\partial X}\right)^2 + \left(\frac{\partial\theta_2}{\partial Y}\right)^2\right] \tag{45a}$$

$$N_s = \frac{\omega^2}{(\omega\theta_s + 1)^2}\left[\xi^2\left(\frac{\partial\theta_s}{\partial X}\right)^2 + \left(\frac{\partial\theta_s}{\partial Y}\right)^2\right] - \frac{\omega Bi(\theta_s - \theta_f)}{\omega\theta_s + 1} \tag{45b}$$

$$N_f = \frac{k\omega^2}{(\omega\theta_f + 1)^2}\left[\xi^2\left(\frac{\partial\theta_f}{\partial X}\right)^2 + \left(\frac{\partial\theta_f}{\partial Y}\right)^2\right] + \frac{\omega Bi(\theta_s - \theta_f)}{\omega\theta_f + 1} + \frac{\omega BrM_d sin^4(\gamma)D_1^2[\cosh(SY_1) - \cosh(SY)]^2}{M(\omega\theta_f + 1)} \tag{45c}$$

$$N_{FF} = \frac{\omega D_1^2 Br\left(1 + \frac{1}{\beta}\right)}{MDa(\omega\theta_f + 1)}[\cosh(SY_1) - \cosh(SY)]^2 + \frac{\omega D_1^2 S^2 Br\left(1 + \frac{1}{\beta}\right)}{(\omega\theta_f + 1)}\sinh^2(SY) \tag{45d}$$

$$N_{DI} = \frac{\varphi}{\Phi}\left[\xi^2\left(\frac{\partial\Phi}{\partial X}\right)^2 + \left(\frac{\partial\Phi}{\partial Y}\right)^2\right] + \frac{\omega\varphi}{\omega\theta_f + 1}\left[\xi^2\left(\frac{\partial\Phi}{\partial X}\right)\left(\frac{\partial\theta_f}{\partial X}\right) + \left(\frac{\partial\Phi}{\partial Y}\right)\left(\frac{\partial\theta_f}{\partial Y}\right)\right] \tag{45e}$$

$$N_{w1} = \frac{k_{e1}\omega^2}{(\omega\theta_1 + 1)^2}\left[\xi^2\left(\frac{\partial\theta_1}{\partial X}\right)^2 + \left(\frac{\partial\theta_1}{\partial Y}\right)^2\right] \tag{45f}$$

$$N_{f,ht} = \frac{k\omega^2}{(\omega\theta_f + 1)^2}\left[\xi^2\left(\frac{\partial\theta_f}{\partial X}\right)^2 + \left(\frac{\partial\theta_f}{\partial Y}\right)^2\right] \tag{45g}$$

$$N_{s,ht} = \frac{\omega^2}{(\omega\theta_s + 1)^2}\left[\xi^2\left(\frac{\partial\theta_s}{\partial X}\right)^2 + \left(\frac{\partial\theta_s}{\partial Y}\right)^2\right] \tag{45h}$$

$$N_{int} = \frac{\omega^2 Bi(\theta_s - \theta_f)^2}{(\omega\theta_s + 1)(\omega\theta_f + 1)} \tag{45i}$$

$$N_{mg} = \frac{\omega BrM_d sin^4(\gamma)D_1^2[\cosh(SY_1) - \cosh(SY)]^2}{M(\omega\theta_f + 1)}, \tag{45j}$$

where dimensional and non-dimensional entropies in Eqs. (44) and (45) have been defined in the nomenclature. Finally, adding all entropy generation sources given by Eqs. (45a) to (45f) and integrating over the entire volume of the microreactor reveals the total entropy generation or the total irreversibility of the system.

$$N_{pm} = N_{f,ht} + N_{s,ht} + N_{int} + N_{mg} + N_{FF} + N_{DI} \tag{46}$$

$$N_{Tot} = \int_{-1}^{1}\int_{0}^{1}\sum N_i dXdY,\ i = w_1, s, f,\ FF,\ DI,\ w_2 \tag{47}$$

It is noted that the formulation of irreversibility in this section excludes the irreversibility of the chemical reaction. Although, in general, chemical reactions can be highly irreversible, the extent of their irreversibility is reaction dependent and thus it has been excluded here. Hence, the calculated total irreversibility can be regarded as a transport irreversibility.

3. Results and discussions

Table 2 shows the basic numerical values of the dimensionless parameters used in this section. Any variation to these values has been specified on the figures or in their captions. In selecting these values, an attempt was made to provide a ground for comparison through using the values already considered in the literature [10,11,14,54] for simpler configurations.

3.1. Validation

Two different and independent approaches are taken to validate the analytical solutions developed in Section 2. First, the predicted temperature fields and Nusselt numbers in the absence of thermal

Table 2
The default values of parameters.

Dimensionless Parameter	Default Value	Dimensionless Parameter	Default Value
Bi	1	Q	0.75
Br	0.01	Q_{w1}	0.5
Da	0.1	Q_{w2}	0.2
Dn	1	ω	0.001
Pe	10	φ	0.01
Pr	5	Y_1	0.8
R	150	ξ	0.05
Sr	0.7	Rd	0
ε	0.95	γ	$\pi/2$
k	0.05	M	1
k_{e1}	0.5	Md	25
k_{e2}	0.2	β	0.5

radiation, magnetic effects and in the limit of high Casson fluid parameter are compared with those reported in Ref. [14]. As depicted by Fig. 2 this reveals an excellent agreement. Second, Appendix B shows that the analytical solution derived in Section 2.3 can be systematically reduced to that of Ting et al. [11] for a porous microchannel. Given these, the current analytical work is deemed valid.

3.2. Heat and mass transfer

Equation 11 provides an analytical solution for the flow velocity. In keeping with the findings of other authors [42,43], the solution of this equation shows that fluid velocity decreases by intensification of magnetic and non-Newtonian effects. Nonetheless, for conciseness reasons, the flow velocity profiles are not reported here. It is worth noting that changes in the rheological characteristics of the fluid can alter magnitude of the flow velocity. However, as long as diffusivity of

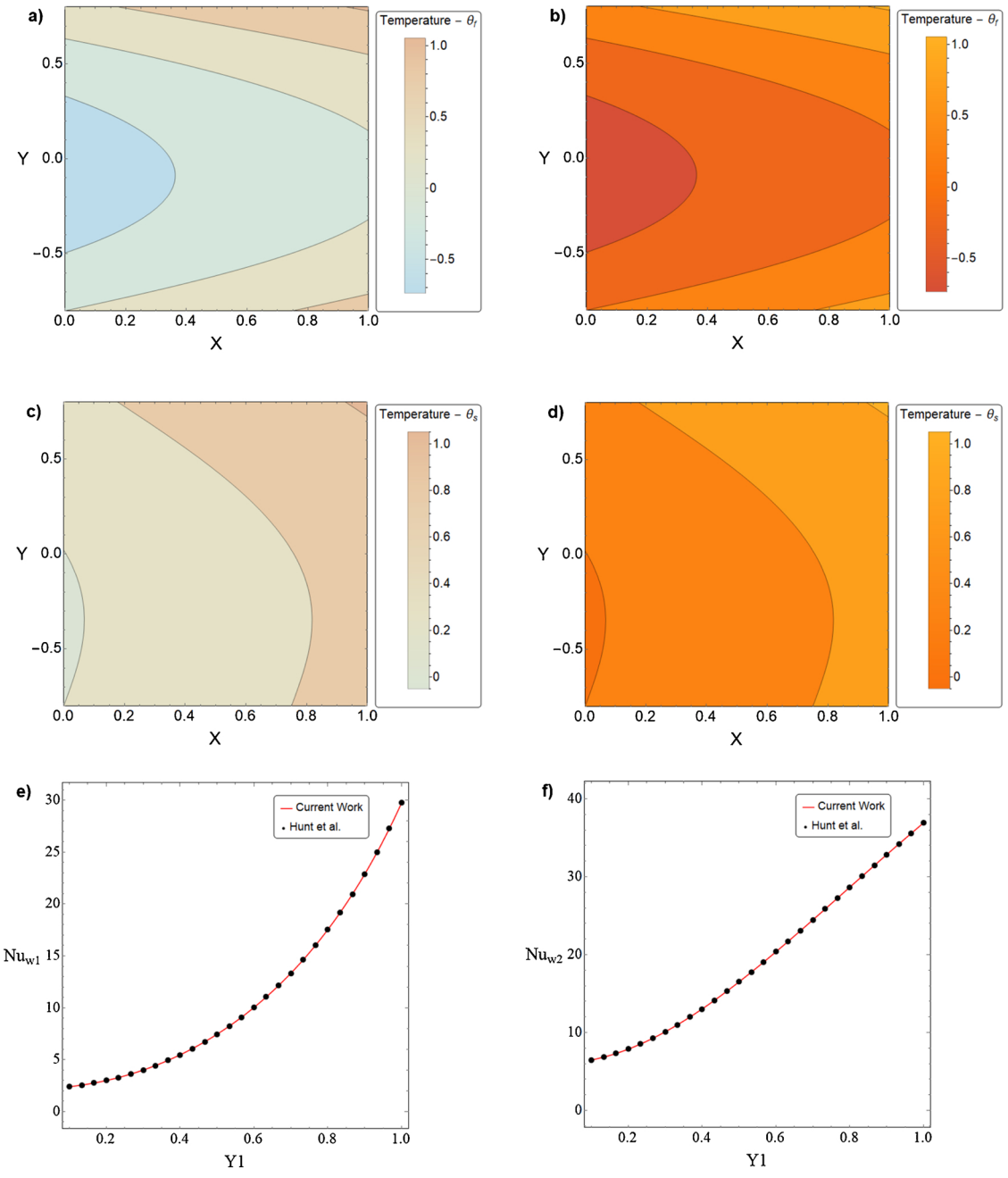

Fig. 2. Comparison of the current analysis (left column) against Hunt et al. [12] (right column). a) and b) the fluid phase temperature contours, c) and d) the solid phase temperature contours, and e) and f) the lower and upper wall Nusselt number, respectively.

the fluid is not significantly changed, the general advective-diffusive features of the system discussed in this section remain mostly unchanged. Figs. 3 and 4 show the contours of temperature in the fluid and solid phases of the microreactor. The general advective-diffusive nature of transport of heat is well reflected by these figures in which dimensionless temperature increases axially while there is strong transversal temperature gradient. This is similar to the earlier temperature predictions of Ting et al. [10,11] in non-reactive porous microchannels. However, the current results also present an asymmetry of the temperature field, which originates from the asymmetry of the surface heat releases. Evidently, such asymmetry is quite strong in the solid phase of the porous medium and is less noticeable in the fluid phase. This is primarily due to the much higher thermal conductivity of the solid phase ($k = 0.05$), making this phase very responsive to imbalance in the surface heat release. Further, Figs. 3 and 4 indicate that, for all investigated cases, there are significant differences between the fluid and solid phase temperatures. This difference clearly demonstrates the necessity of employing LTNE approach in the current analysis

Fig. 3 also shows the influences of magnetic field upon the temperature distributions. According to this figure, intensification of the

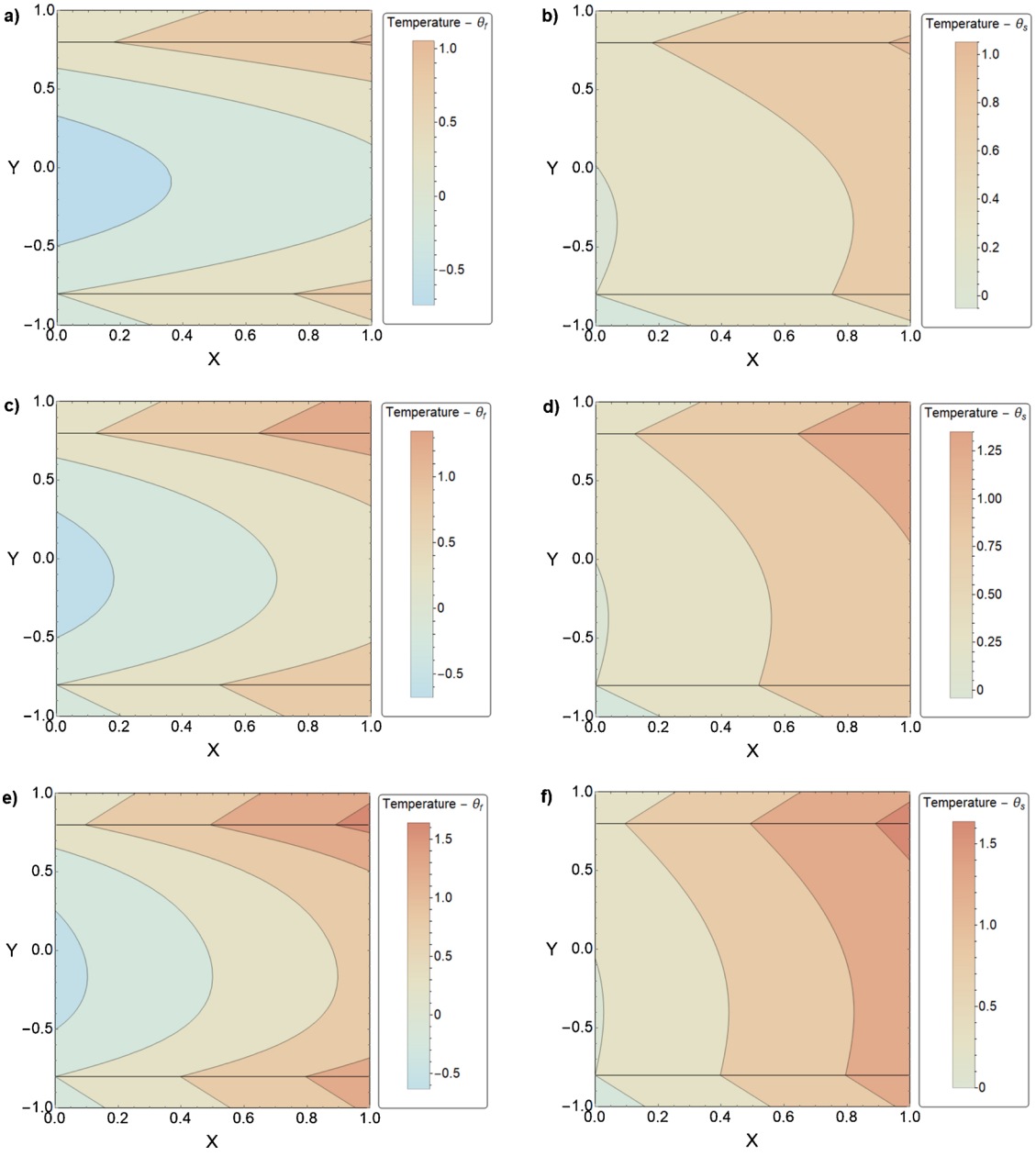

Fig. 3. Temperature contours with varying values of magnetic field intensity, M_d – a), c) and e) fluid temperature contours with M_d of 0, 25 and 50, respectively. b), d) and f) temperature contours of the solid phase with M_d of, 0, 25 and 50, respectively.

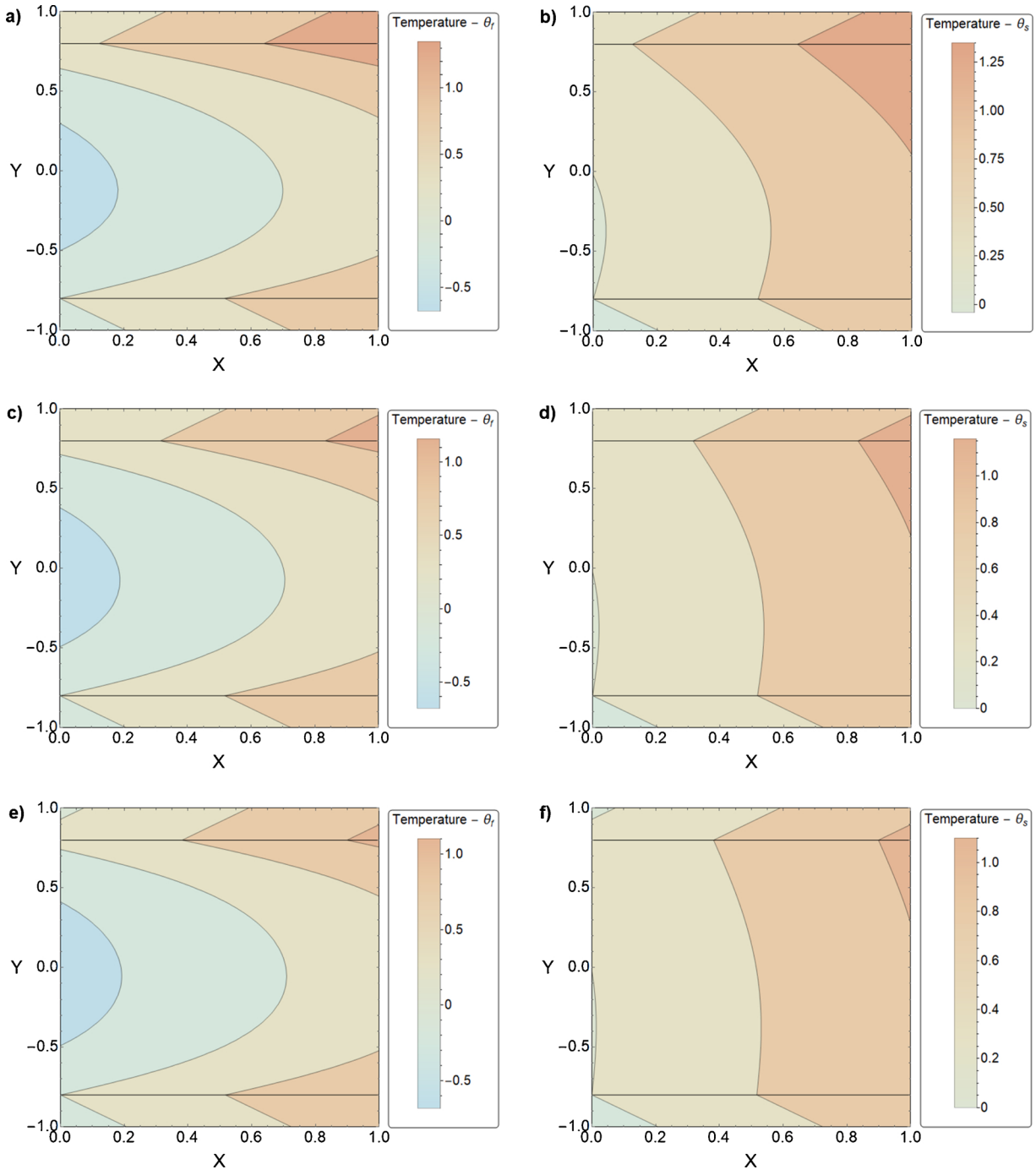

Fig. 4. Temperature contours for varying values of radiation parameter, R_d – a), c) and e) temperature contours of fluid phase with R_d of 0, 1, and 2, respectively. b), d) and f) temperature contours of the solid phase with R_d of 0, 1, and 2, respectively.

magnetic field results in increasing the dimensionless temperature at the outlet of the microchannel. This trend can be consistently observed in both fluid and solid phases. It will be later shown that increasing the intensity of the magnetic field results in enhancement of convective heat transfer coefficient. It is well-known that in forced convection, increases in the loss of momentum boosts the rate of heat transfer [50]. It is therefore reasonable to anticipate an enhancement in the transfer of heat to the fluid and thus a wider range of transversal temperature changes at higher magnetic intensities. As the temperatures of the solid and fluid phases in the porous medium are coupled through internal heat exchanges, an increase in the fluid temperature also elevates the solid temperature. This can be readily seen in the dimensionless temperature of the solid phase in Fig. 3. This figure also shows that by increasing the magnetic field the general shape of the temperature contours changes and it becomes flatter. This is because of the influences of magnetic field (through Lorentz force) upon the fluid velocity [20,42], which slows it down and makes the profile flatter and renders the same effect on the temperature fields.

The effects of thermal radiation on the temperature fields are depicted by Fig. 4. This figure shows that increasing the thermal radiation parameter from zero to two imparts only slight effects on the temperature contours. This may sound counter intuitive. However, it will be later shown that in the current asymmetric problem, thermal radiation has opposing effects on the top and bottom surfaces of the

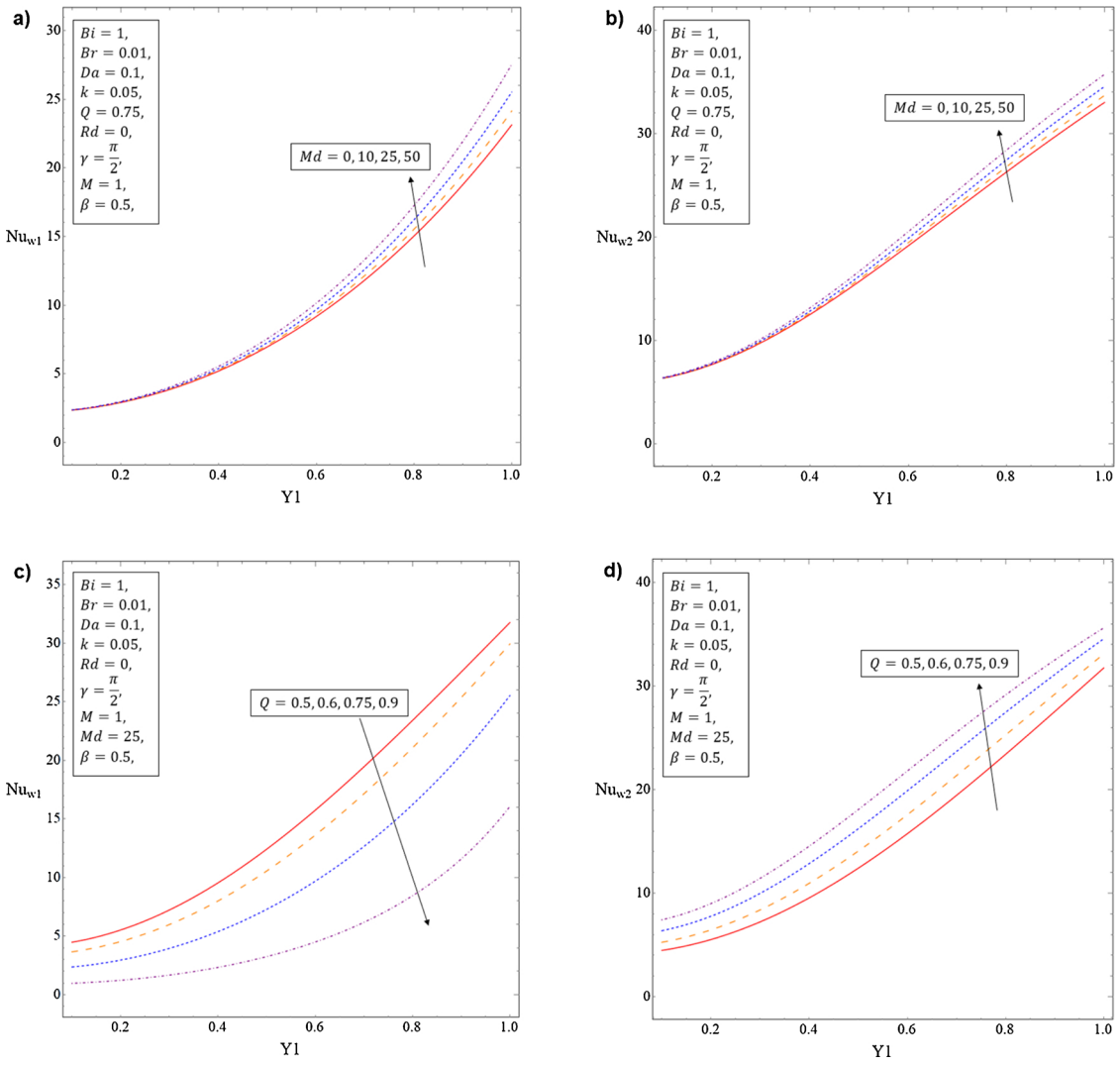

Fig. 5. Nusselt Number against wall thickness, Y_1. a) and b) varying magnetic interaction parameter, M_d, for the lower and upper wall, respectively. c) and d) varying heat flux ratio, Q, for the lower and upper wall, respectively.

microchannel. These two largely cancel each other and thus minimise the effects of thermal radiation on the temperature fields. Despite this, a small decrease in the extent of axial temperature variation along the microchannel is evident in Fig. 4.

Fig. 5 shows the variation of Nusselt number as a function of the dimensionless microchannel height (Y_1). This figure shows that, in general, increases in the dimensionless microchannel height, or making the microchannel wall thinner, results in a significant increase in Nusselt number. This is to be expected as the thickness of the microchannel wall introduces a thermal resistance and reduces the rate of heat transfer [14,23,44]. Fig. 5a and b indicate that increases in the intensity of the magnetic field enhances the value of Nusselt number on both top and bottom walls. The physical reason for this increase was already explained. Yet, Figs. 5a and b indicate that the extent of heat transfer enhancement by the magnetic field is dependent upon the wall thickness. At low values of Y_1 (indicating thick walls of the microreactor), changes in the intensity of magnetic field imparts hardly any effect on the Nusselt number. Nonetheless, as the height and thickness of the microchannel approach each other the enhancement of heat transfer coefficient with the magnetic field becomes more noticeable. In the limit of thick walls, the heat transfer in the system is dominated by conduction in the walls. Since magnetic field has no influence on the conduction across the walls, thick wall microreactor becomes almost indifferent to intensification of magnetic field. This finding is of practical significance as many real microreactors have thick-walls [6] and hence, ignoring the wall in their thermal analysis can lead to erroneous results.

Fig. 5c and d show that increases in the heat flux ratio (as defined in Table 1) can have opposite effects on the Nusselt numbers on the bottom and top walls of the microreactor. Heat flux ratio is essentially the ratio of the surface heat release that enters the porous region from the top and bottom catalytic surfaces (see Fig. 1 and Table 1). A value of 0.5 indicates similarity of the heat release on the two catalytic surfaces, while values between 0.5 and 1 imply stronger heat release on the top

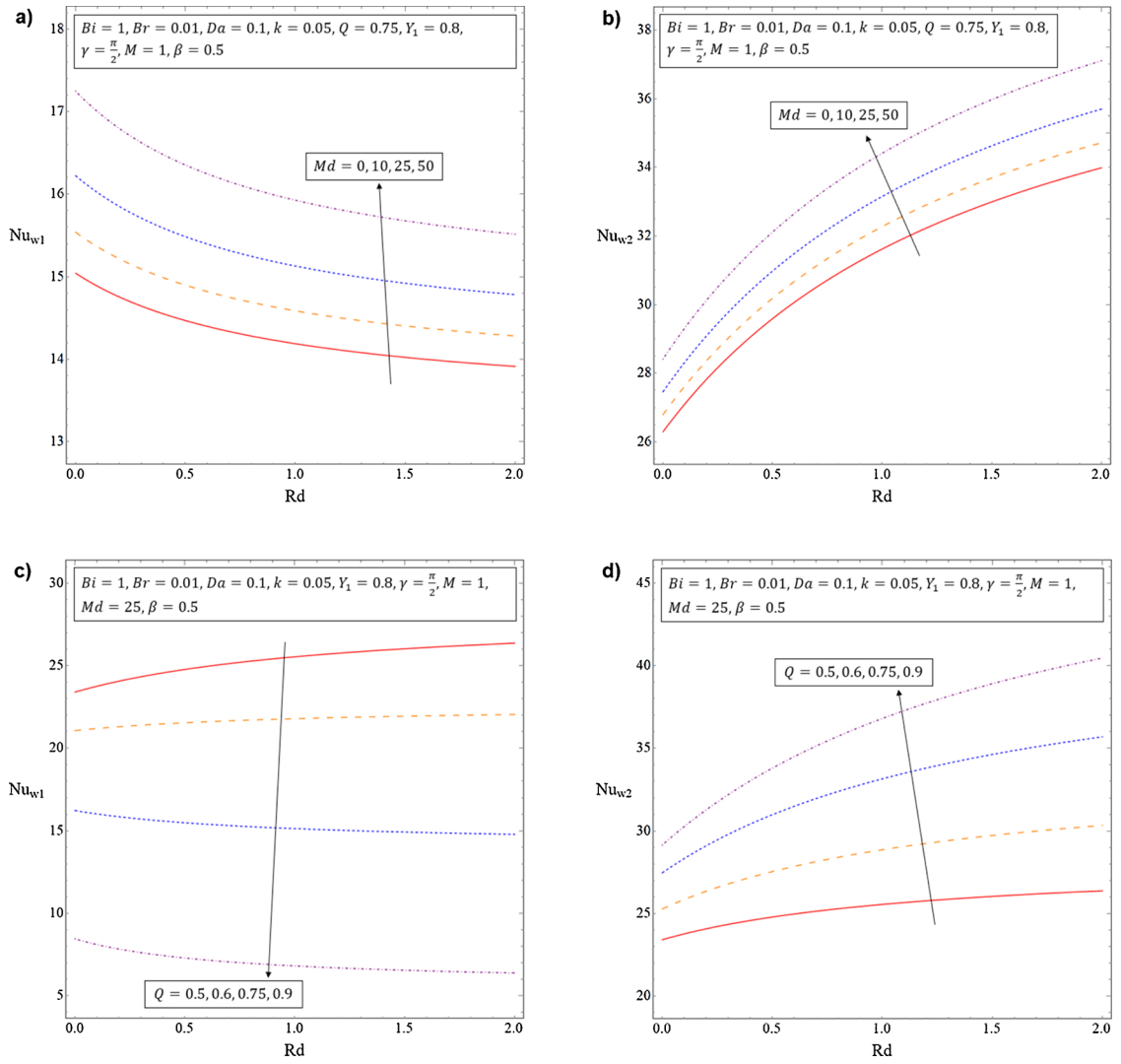

Fig. 6. Nusselt Number against radiation parameter, R_d. a) and b) show varying magnetic interaction parameter, M_d, for the lower and upper wall, respectively. c) and d) heat flux ratio, Q, for the lower and upper wall, respectively.

surface and those between 0 and 0.5 mean more heat release on the bottom surface. Figs. 5c and d show that by increasing the surface heat release on the top surface the Nusselt number of the bottom surface decreases considerably, while that of the top surface increases. The physics of this behaviour can be explained as follows. A stronger surface heat release on the top surface establishes a transversal conduction of heat between the two catalytic surfaces mainly through the solid phase of the porous medium. Such conduction of heat from the top to bottom surface diminishes the transversal temperature gradient around the bottom surface where a smaller heat flux is dissipated. This results in reduction of the heat transfer coefficient on the bottom surface of the microchannel. In the same way, strengthening the transversal temperature gradient on the top wall magnifies the rate of heat transfer and enhances the value of Nusselt number.

The responses of Nusselt number to varying the value of radiation parameter are shown in Fig. 6. It is clear from this figures that radiation affects the top and bottom walls differently. As of Fig. 5, this is due to the asymmetry of surface heat release. In general, for the wall with stronger surface heat release (top wall in Fig. 6) increases in thermal radiation parameter enhances the value of Nusselt number significantly. An explanation for this trend could be offered by recalling that in the current setting radiation is an added conductivity. Increases in the radiation parameter effectively increases the conductivity of porous medium and it therefore intensifies the processes explained in the discussions regarding Fig. 5. Previous works on the influences of radiation in microreactors with homogeneous exothermic reactions showed that increases in thermal radiation causes a uniform increase in Nusselt number [23]. However, Fig. 6 implies that this is no longer the case in microreactors with dissimilar surface reactions. Interestingly, Fig. 6c shows that in the case of similar surface reactions ($Q = 0.5$) the behaviour of microreactors with homogenous reactions are retrieved. Fig. 6 further shows that the intensity of magnetic field and the heat flux ratio (Q, as defined in the nomenclature) can majorly influence the value of Nusselt number. Once again, the trend of variation is different on the walls with higher and lower surface heat release.

The developed analytical solution in Section 2 for mass transport,

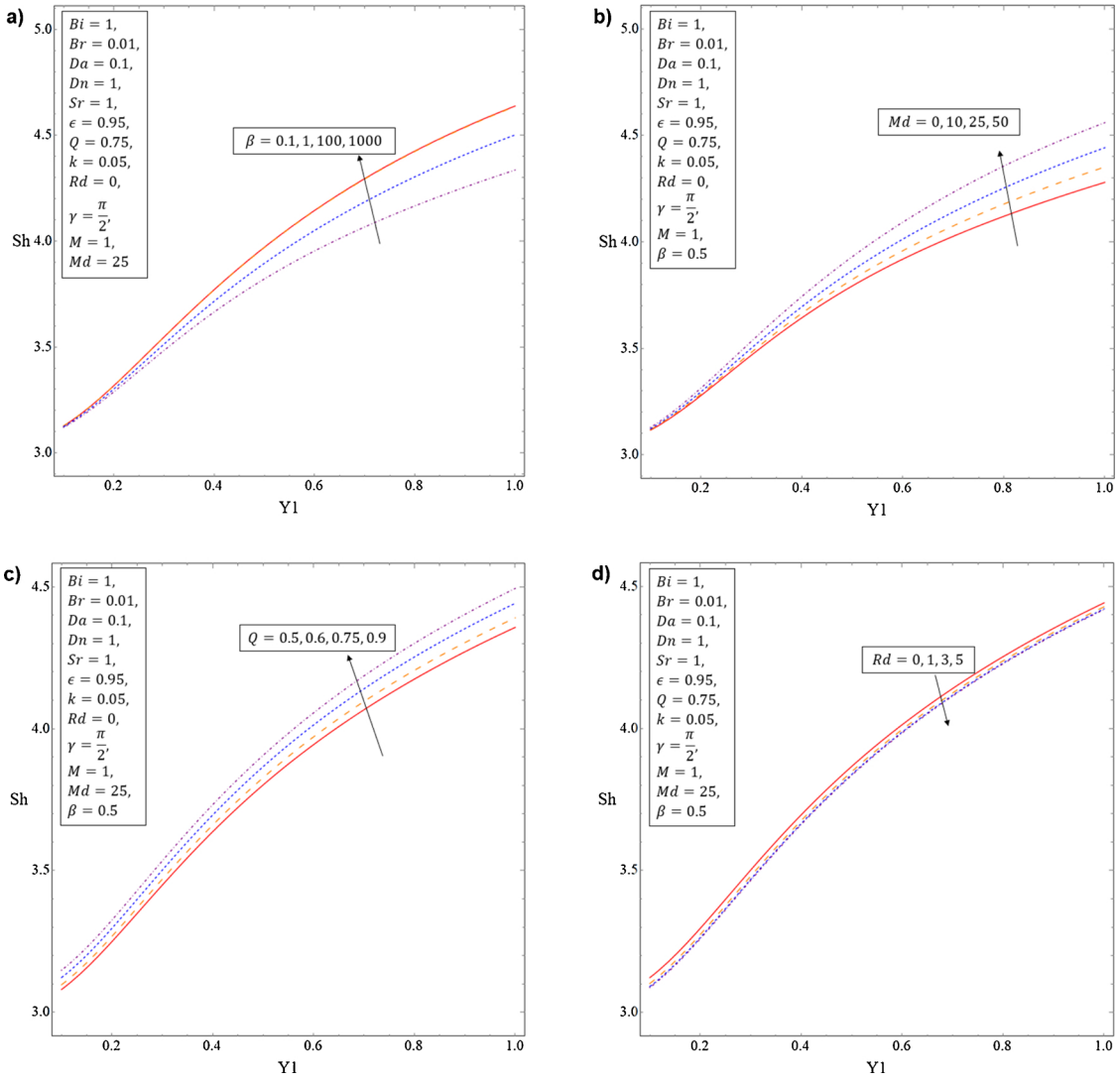

Fig. 7. Sherwood Number against wall thickness, Y_1. a), b), c), and d) varying Casson fluid parameter, β, magnetic interaction parameter, M_d, heat flux ratio, Q, and radiation parameter, R_d, respectively.

provides a two-dimensional view of the concentration field. Nonetheless, for the reasons of brevity the concentration fields are not shown here and instead Sherwood number is discussed. Fig. 7 shows that the microreactor wall thickness affects Sherwood number in an analogous way to its influence upon Nusselt number. This is due to the wall thermal effects, which manifest themselves in Sherwood number through thermal diffusion of mass (see the advective-diffusive Eq. (7)). It is important to note that although there is a qualitative similarity between Figs. 7 and 5, the extent of changes in Nusselt number with Y_1 is significantly larger than that of Sherwood number. This is to be expected, as heat transfer introduces a secondary effect upon mass transfer while the Fickian diffusion of mass remains insensitive to wall thickness. In keeping with this argument, Figs. 7b shows that magnetic effects can only slightly enhance the rate of mass transfer. Once again, this is related to enhancement/suppression of heat transfer, which then affect the transfer of mass through Soret effect.

Fig. 7a shows the influences of Casson fluid parameter upon Sherwood number. Lower values of Casson fluid parameter indicate deviation from Newtonian fluid behaviour. This, in turn, affects the advection of mass and thus influences Sherwood number. Fig. 7a shows that Sherwood number is maximised at high values of Casson fluid corresponding to Newtonian fluid. This implies that non-Newtonian properties of the fluid tend to suppress the mass transfer process. More viscous nature of Casson fluid hinders the advection of mass and therefore reduces the mass transfer coefficient and Sherwood number. Also, although not shown here, decreases in Casson fluid parameter slightly reduces the rate of heat transfer and thus decreases Sherwood number through thermal diffusion effects. This explains the observed dependency of Sherwood number on the wall thickness in Fig. 7a. Fig. 7c further indicates that asymmetry of surface heat release and thermal radiation slightly enhance Sherwood number, while the influences of thermal radiation are quite small. The secondary heat transfer

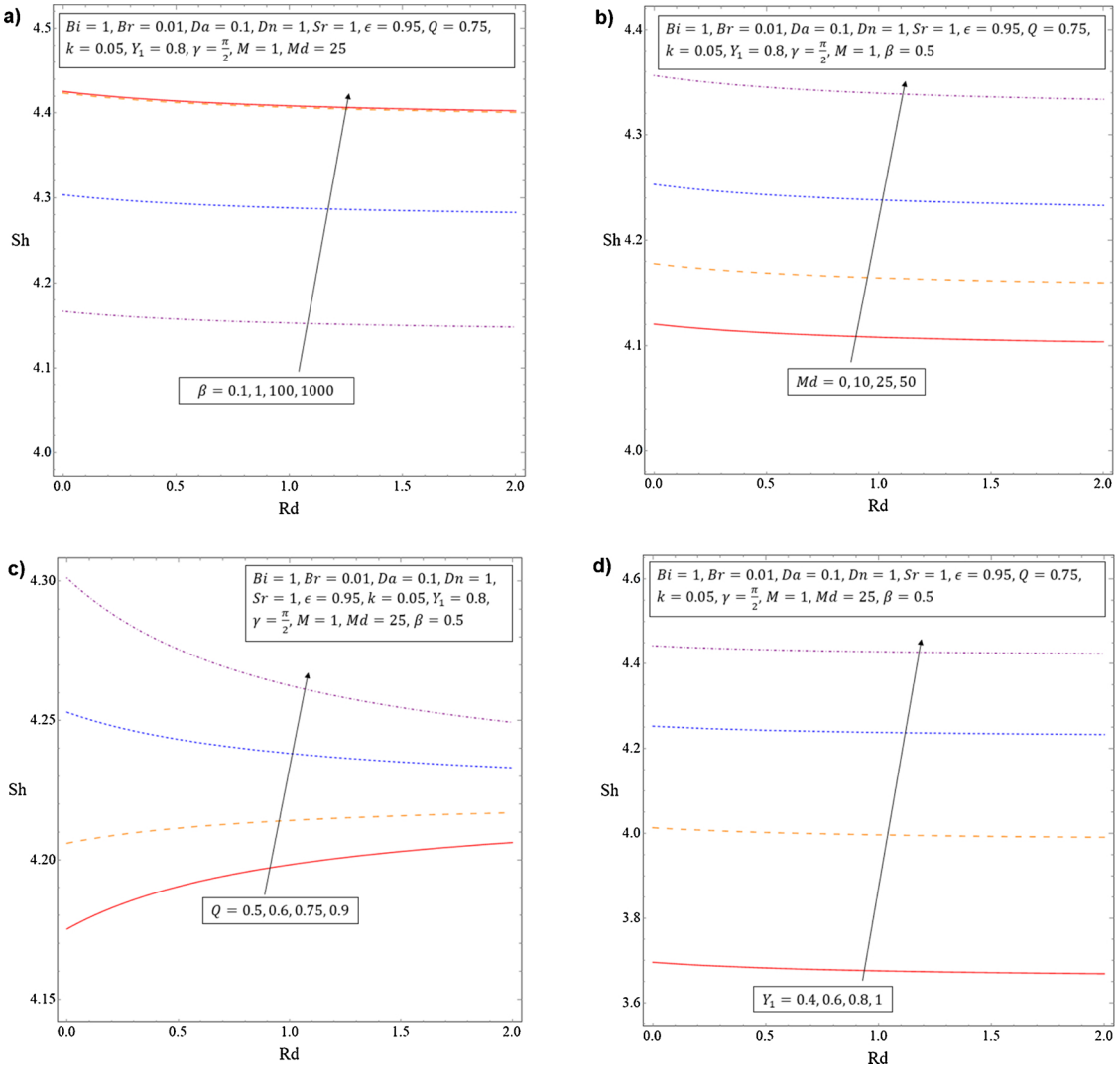

Fig. 8. Sherwood Number against radiation parameter, R_d. a), b), c), and d) varying Casson fluid parameter, β, magnetic interaction parameter, M_d, heat flux ratio, Q, and wall thickness, Y_1, respectively.

effects upon mass transfer are the reason for the observed trends in these two figures.

Fig. 8 explores the effects of radiation parameter on Sherwood number. It is observed that Sherwood number is generally rather insensitive to the intensity of thermal radiation. Nonetheless, a small dependency between the two exists at low values of radiation parameter in which Sherwood number slightly drops by increases in the value of radiation parameter (see Figs. 8a and b). Fig. 8c, however, shows that strong asymmetry of surface heat release can totally change this trend. According to this figure, depending on the value of heat flux ratio, thermal radiation can either enhance or suppress Sherwood number. Further, Fig. 8a shows that, as already discussed, lowering the value of Casson parameter results in the suppression of Sherwood number. However, upon capturing the Newtonian fluid properties at higher values of Casson fluid parameter, Sherwood number becomes indifferent to Casson fluid parameter. Also, Figs. 8b and d, once again, depict the enhancement of mass transfer by intensifying the magnetic field and making the walls thinner.

As a closing remark, it is noted that in the current analysis the assumed zeroth-order catalytic reaction decouples the catalyst from mass transfer process. However, in the case of higher order reactions the catalytic activity is influenced by mass transfer and thus the trends discussed in Figs. 7 and 8 can affect the reactions and surface heat release. Yet, it was shown that modification of heat release could influence heat and mass transfer. This indicates that in this problem there is a possibility for the existence of sophisticated transport-chemistry interactions that are still unexplored.

3.3. Thermodynamic irreversibilities

The total entropy generation calculated by Eq. (47) is shown in Fig. 9. This figure indicates that, in general, thickening of the walls of microreactor and suppression of thermal radiation result in an increase in the entropy generation. This is to be expected as both effects hinder heat transfer processes and thus strengthen the temperature gradients in the system, which then contribute strongly with entropy generation.

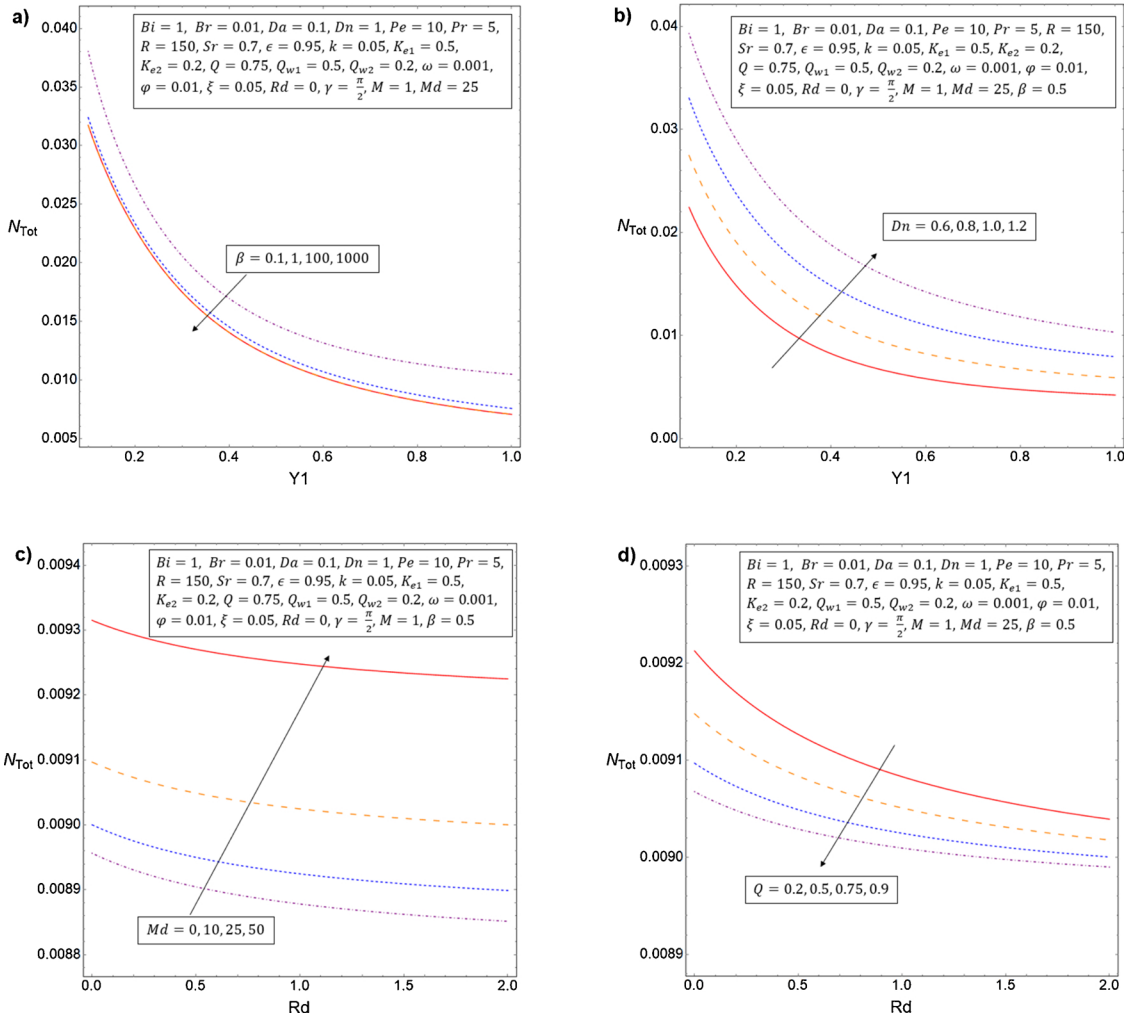

Fig. 9. Total Entropy against wall thickness, Y_1, (Top row) and Radiation parameter, R_d, (Bottom row). a), b), c), and d) varying Casson fluid parameter, β, Damköhler number, D_n, magnetic interaction parameter, M_d, and heat flux ratio, Q.

Further, increases in Casson fluid parameter appears to be influential on the total entropy generation of the system with its lower values tending to increase the irreversibility (see Fig. 9a). As already discussed, lower values of Casson fluid are associated with more viscous and less heat transferring flow. These contribute with the frictional and thermal irreversibilities of the system and hence increase the total entropy generation. Further, Fig. 9b indicates that Damköhler number can considerably affect the total irreversibilities of the problem. This is an expected result as the rate of reaction and mass diffusivities are amongst the key parameters dominating the process of mass transfer and thus its associate irreversibility. Figs. 9c and 9d imply that the effects of heat flux ratio and intensity of magnetic field on the total entropy generation are quite small (note the scale in these two figures).

Figs. 10 and 11 provide the spatial distribution of entropy generation by different sources of irreversibly and depict the distribution of total entropy generation with the porous medium (that is the total entropy generation within the system minus the irreversibility in the reactor walls). Fig. 10 shows that entropy generation by fluid friction is mostly generated in the vicinity of the walls where there is a strong shear dispersion of the flow. There is also an area with large frictional irreversibility along the centreline of the microchannel in which fluid velocity is maximum. In a channel flow this corresponds to a region with considerable velocity gradient and thus frictional losses [48,50]. Fig. 11 illustrates the effects of the intensity of magnetic field on the entropy generation field. Intensification of magnetic field mostly influences the central region of the microchannel and reduces the irreversibility of that area. This could be due to the flow retardation effect of the magnetic field. It is well-demonstrated that magnetic field decelerates the fluid flow and suppresses development of high velocity regions of the flow. It, therefore, cancels out formation of strong velocity gradients and reduces entropy generation. At the same time, strengthening of the magnetic field improves the rate of heat transfer and hence smears out the temperature gradients and suppresses the thermal entropy generation. The general behaviour of total entropy generation in the porous medium shown in Figs. 10 and 11 is consistent with those discussed for non-exothermic catalytic microreactors [44]. It has been shown that the total entropy generation in catalytic microreactors is dominated by mass transfer [44]. This appeared to remain valid in exothermic catalytic microreactors with reasonable values of surface heat release. Since it was already shown that heat transfer only

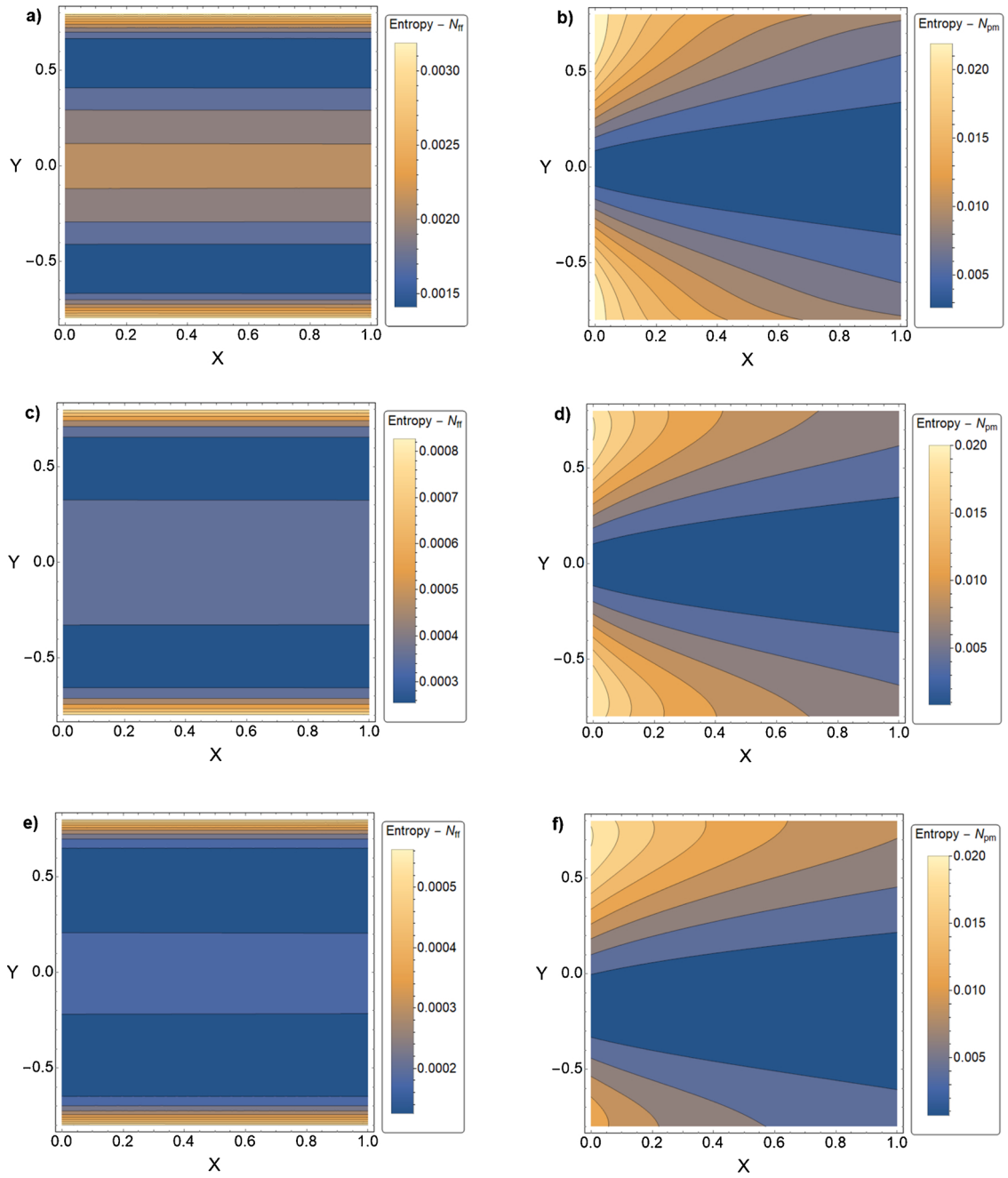

Fig. 10. Local Entropy contours with varying values for the Casson fluid parameter, β, at a wall thickness of 0.2. a), c), and e) show the local entropy field for N_{FF} with β equal to 0.1, 1 and 1000, respectively. b), d), and f) show the local entropy field for N_{pm} with β equal to 0.1, 1 and 1000, respectively.

moderately affects mass transfer, the reader is referred to the discussion in Refs [14,44]. about the distribution of total entropy generation.

4. Conclusions

The problem of surface heat release on the internal walls of a microreactor, filled by a porous medium, was tackled analytically. Previous studies have shown that the porous medium in such configuration is far from local thermal equilibrium and thus a non-equilibrium approach is needed for modelling the transport processes. However, none of the conventional porous-solid interface models could be used in this case. To address this issue, a novel porous-solid interface model was developed in the current work. This was an extension to the recent work of the authors [14] by including the effects of thermal radiation in the interface model. The new model was then used in a two-dimensional analytical study of porous catalytic microreactors with magnetic and non-Newtonian fluid effects. Such configuration is a simplified representations of magnetic biofuel micro-reformers and other magnetic, porous catalytic microreactors. The theoretical work was validated through a rigorous and systematic reduction of the derived expressions to the existing solutions developed for simpler configurations.

The key physical findings of this work can be summarised as follows.

- Asymmetry in catalytic surface heat release could affect Nusselt and Sherwood number significantly.
- Magnetic field and thermal radiation could either increase or decrease Nusselt number depending upon the asymmetry of surface heat release.

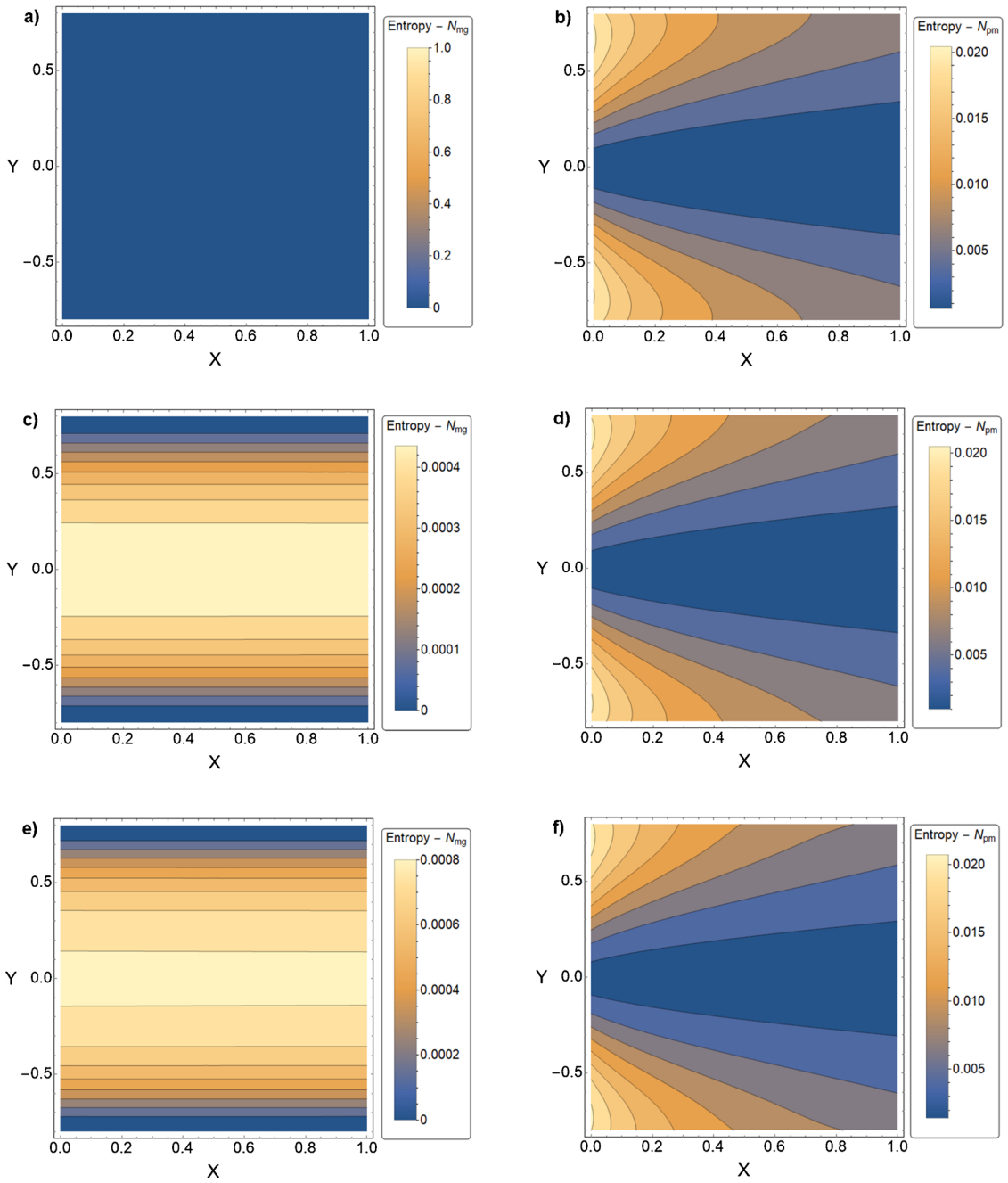

Fig. 11. Local Entropy contours with varying values of magnetic field intensity, M_d, at a wall thickness of 0.2. a), c), and e) show the local entropy contours for N_{mg} with M_d equal to 0, 25 and 50, respectively. b), d) and f) show the local entropy field for N_{pm} with M_d equal to 0, 25 and 50, respectively.

- In the thick wall limit ($Y_1 < 0.5$), the thermal response of micro-reactor is dominated by heat conduction and hence magnetic field has little effect on heat transfer.
- Asymmetry of surface heat release results in strengthening of transversal temperature gradients around the more exothermic surface, while it reduces the gradient on the less exothermic surface. This enhances the rate of heat transfer on the surface with stronger catalytic heat release and suppresses that on the surface with less heat release.
- The total entropy generation within the microreactor was found to be strongly influenced by the thickness of the wall. In general, thicker walls significantly intensify the generation of entropy.
- Amongst all investigated parameters, Damköhler number was found to have the strongest effects upon generation of entropy, indicating the dominance of irreversibility by mass transfer.
- Intensification of Casson fluid characteristic of the flow (decreasing Casson fluid parameter) reduces Sherwood number and total entropy generation within the microreactor.

The results imply that in the case of higher order kinetics, there could be complex two-way interactions between catalytic heat release and transport processes. This remains as an interesting research avenue to be explored in future. It is, finally, imperative to recall that the developed interface model can be used in both theoretical and numerical analyses of micro and macro catalytic chemical reactors.

Acknowledgment

Nader Karimi acknowledges the partial support of EPSRC through grant numberEP/N020472/1.

Appendix A. Closed Form Constants

$$D_1 = \frac{SY_1}{SY_1\cosh(SY_1) - \sinh(SY_1)},\quad D_2 = \frac{D_1^2 BrM_d}{2M}\sin^4(\gamma) \tag{A1a,b}$$

$$D_3 = \frac{D_1^3 BrM_d}{Y_1 M}\sin^4(\gamma)\left[Y_1\cosh^2(SY_1) + \frac{SY_1 - 3\cosh(SY_1)\sinh(SY_1)}{2S}\right] + \frac{D_1}{2Y_1} - \frac{2D_1^2 BrM_d}{M}\sin^4(\gamma)\cosh(SY_1) \tag{A1c}$$

$$D_4 = \frac{D_1^2 BrM_d}{M}\sin^4(\gamma)\left[\frac{1}{2} + \cosh^2(SY_1)\right] - \frac{D_1}{2Y_1}\cosh(SY_1) - \frac{D_1^3 BrM_d}{Y_1 M}\sin^4(\gamma)\left[Y_1\cosh^2(SY_1) + \frac{SY_1 - 3\cosh(SY_1)\sinh(SY_1)}{2S}\right]\cosh(SY_1) \tag{A1d}$$

$$Q_1 = \frac{Bi(1+k+R_d)}{k(1+R_d)},\quad Q_2 = \frac{4S^2(1+R_d) - Bi}{k(1+R_d)}D_2,\quad Q_3 = \frac{S^2(1+R_d) - Bi}{k(1+R_d)}D_3 \tag{A2a,b,c}$$

$$Q_4 = \frac{BiD_4}{k(1+R_d)},\quad Q_5 = \frac{BiD_2}{k(1+R_d)},\quad Q_6 = \frac{BiD_3}{k(1+R_d)} \tag{A2d,e,f}$$

$$E_1 = \theta_{w2} + \frac{Q_{w2}Y_1}{k_{e2}},\quad E_2 = -\frac{Q_{w2}}{k_{e2}} \tag{A3a,b}$$

$$E_3 = -\frac{Q_2}{16S_4 - 4Q_1S^2},\quad E_4 = -\frac{Q_3}{S^4 - Q_1S^2} \tag{A3c,d}$$

$$E_5 = -\frac{[(D_2 + 4S^2E_3k)\cosh(2SY_1) + (D_3 + S^2E_4k)\cosh(SY_1) + (D_4 + 2E_6k)]\mathrm{sech}(\alpha Y_1)}{k\alpha^2} \tag{A3e}$$

$$E_6 = -\frac{Q_4}{2Q_1},\quad E_7 = \frac{\theta_{w2}}{2Y_1} \tag{A3f,g}$$

$$E_8 = -[E_3\cosh(2SY_1) + E_4\cosh(SY_1) + E_5\cosh(\alpha Y_1) + E_6Y_1^2 - E_7Y_1] \tag{A3h}$$

$$E_9 = \frac{Q_5}{16S^4 - 4Q_1S^2},\quad E_{10} = \frac{Q_6}{S^4 - Q_1S^2} \tag{A3i,j}$$

$$E_{11} = -\frac{[(4S^2E_9)\cosh(2SY_1) + (S^2E_{10})\cosh(SY_1) + 2E_6]\mathrm{sech}(\alpha Y_1)}{\alpha^2} \tag{A3k}$$

$$E_{12} = -[E_9\cosh(2SY_1) + E_{10}\cosh(SY_1) + E_{11}\cosh(\alpha Y_1) + E_6Y_1^2 - E_7Y_1] \tag{A3l}$$

$$E_{13} = \frac{Q_{w1}Y_1}{k_{e1}},\quad E_{14} = \frac{Q_{w1}}{k_{e1}} \tag{A3m,n}$$

$$\text{Where: } \theta_{w2} = \frac{2Y_1}{1+k+R_d}\begin{bmatrix} Q - \sinh(2SY_1)[2SkE_3 + 2SE_9(1+R_d)] - \sinh(SY_1)[SkE_4 + SE_{10}(1+R_d)] - \\ \sinh(\alpha Y_1)[\alpha kE_5 + \alpha E_{11}(1+R_d)] - Y_1[2kE_6 + 2E_6(1+R_d)] \end{bmatrix} \tag{A3o}$$

$$F_1 = \frac{Srk}{\varepsilon Y_1}E_3,\quad F_2 = \frac{Srk}{\varepsilon Y_1}E_4 - \frac{D_1Dn}{Y_1^2S^2},\quad F_3 = \frac{Srk}{\varepsilon Y_1}E_5 \tag{A4a,b,c}$$

$$F_4 = \frac{Srk}{\varepsilon Y_1}E_6 + \frac{D_1Dn}{2Y_1^2}\cosh(SY_1),\quad F_5 = \frac{Srk}{\varepsilon Y_1}E_7 \tag{A4d,e}$$

$$F_6 = \frac{Srk}{\varepsilon Y_1}E_8 + 1 - D_1\left(\frac{Y_1^2}{2}\cosh(SY_1) - \frac{\cosh(SY_1)}{S^2}\right)\frac{Dn}{Y_1^2} - \frac{Srk}{\varepsilon Y_1}\theta_f(-Y_1), \quad \textit{where } \theta_f(-Y_1) = E_3\cosh(2SY_1) + E_4\cosh(SY_1) + E_5\cosh(\alpha Y_1) + E_6Y_1^2 - E_7Y_1 + E_8 \tag{A4f}$$

Appendix B. Validation

The mathematical model presented in this work is validated against the analytical solution of Ting et al. [11] and Hunt et al. [14]. As the magnetic parameter, magnetic field angle and the volumetric source term approach zero and the Casson fluid parameter tends to infinity, the model can be compared to that in Hunt et al. [14] without viscous dissipation. To produce a model equivalent to that analysed in Hunt et al. [14], all Casson fluid terms are either set to 0 or infinity and the volumetric source term is also eliminated. This reduces the momentum and heat transfer equations to that shown below.

$$-\frac{\partial p}{\partial x} + \mu_{eff}\frac{\partial^2 u}{\partial y^2} - \frac{\mu_{nf}}{\kappa}u = 0 \quad -h_1 \le y < h_1 \tag{B1a}$$

$$k_{enf}\frac{\partial^2 T_{nf}}{\partial y^2} + h_{sf}a_{sf}(T_s - T_{nf}) = \rho_{nf}C_{p,nf}u\frac{\partial T_{nf}}{\partial x} \quad -h_1 \le y < h_1 \tag{B1b}$$

$$k_{es}\frac{\partial^2 T_s}{\partial y^2} - h_{sf}a_{sf}(T_s - T_{nf}) = 0 \quad -h_1 \le y < h_1 \tag{B1c}$$

Using the new momentum and heat transfer equations, Eq.17 becomes:

$$\frac{dT_{nf}}{dx} = \frac{q_1 + q_2}{2\rho_{nf}C_{p,nf}uh_1} \tag{B2}$$

The new dimensionless temperature ODE's become:

$$\theta_{nf}'''' - Q_1'\theta_{nf}'' + Q_3'\cosh(SY) - Q_4' = 0 \tag{B3a}$$

$$\theta_s'''' - Q_1'\theta_s'' - [Q_6'\cosh(SY) + Q_4'] = 0 \tag{B3b}$$

$$\theta_{nf}(Y) = E_4'\cosh(SY) + E_5'\cosh(\alpha Y) + E_6'Y^2 + E_7'Y + E_8' \quad -Y_1 \le Y < Y1 \tag{B4a}$$

$$\theta_s(Y) = E_{10}'\cosh(SY) + E_{11}'\cosh(\alpha Y) + E_6'Y^2 + E_7'Y + E_{12}' \quad -Y_1 \le Y < Y1 \tag{B4b}$$

$$\alpha' = \sqrt{Q_1'} \tag{B4c}$$

$$\frac{d\theta_{nf}}{dX} = \Omega' = \frac{1}{k_s'Y_1PrRe} \tag{B5}$$

$$\theta_{nf}(X,Y) = E_4'\cosh(SY) + E_5'\cosh(\alpha Y) + E_6'Y^2 + E_7'Y + E_8' + \Omega X \quad -Y_1 \le Y < Y1 \tag{B6a}$$

$$\theta_s(X,Y) = E_{10}'\cosh(SY) + E_{11}'\cosh(\alpha Y) + E_6'Y^2 + E_7'Y + E_{12}' + \Omega'X \quad -Y_1 \le Y < Y1 \tag{B6b}$$

The Nusselt number equations become:

$$Nu_{w1}' = \frac{2Y_1(Q-1)}{k\theta_{nf}'} \tag{B7a}$$

$$Nu_{w2}^{'} = \frac{2QY_1}{k(\theta_{w2}^{'} - \bar{\theta}_{nf}^{'})} \quad \text{(B7b)}$$

$$\bar{\theta}_{nf}^{'} = \frac{D_1^{'}}{2Y_1}\int_{-Y_1}^{Y_1} \theta_{nf}^{'}[\cosh(SY_1) - \cosh(SY)]dY \quad \text{(B8)}$$

Where the constants, $Q^{'}$ and $E^{'}$ are defined by:

$$D_1^{'} = \frac{SY_1}{SY_1\cosh(SY_1) - \sinh(SY_1)},\ D_2^{'} = 0,\ D_3^{'} = \frac{D_1^{'}}{2Y_1},\ D_4^{'} = -\frac{D_1^{'}}{2Y_1}\cosh(SY_1) \quad \text{(B9a,b,c,d)}$$

$$Q_1^{'} = \frac{Bi(1+k)}{k},\ Q_2^{'} = 0,\ Q_3^{'} = \frac{S^2 - Bi}{k}D_3^{'} \quad \text{(B10a,b,c)}$$

$$Q_4^{'} = \frac{BiD_4^{'}}{k},\ Q_5^{'} = 0,\ Q_6^{'} = \frac{BiD_3^{'}}{k} \quad \text{(B10d,e,f)}$$

$$E_4 = -\frac{Q_3^{'}}{S^4 - Q_1^{'}S^2},\ E_5 = -\frac{[(D_3^{'} + S^2E_4^{'}k)\cosh(SY_1) + (D_4^{'} + 2E_6^{'}k)]\mathrm{sech}(\alpha^{'}Y_1)}{k\alpha^{'2}} \quad \text{(B11a,b)}$$

$$E_6 = -\frac{Q_4^{'}}{2Q_1^{'}},\ E_7 = \frac{\theta_{w2}^{'}}{2Y_1},\ E_8 = -[E_4^{'}\cosh(SY_1) + E_5^{'}\cosh(\alpha^{'}Y_1) + E_6^{'}Y_1^2 - E_7^{'}Y_1] \quad \text{(B11c,d,e)}$$

$$E_{10} = \frac{Q_6^{'}}{S^4 - Q_1^{'}S^2},\ E_{11} = -\frac{[(S^2E_{10}^{'})\cosh(SY_1) + 2E_6^{'}]\mathrm{sech}(\alpha^{'}Y_1)}{\alpha^{'2}} \quad \text{(B11f,g)}$$

$$E_{12} = -[E_{10}^{'}\cosh(SY_1) + E_{11}^{'}\cosh(\alpha^{'}Y_1) + E_6^{'}Y_1^2 + E_7^{'}Y_1] \quad \text{(B117h)}$$

where $\theta_{w2} = \frac{2Y_1}{1+k}[Q - \sinh(SY_1)[SkE_4^{'} + SE_{10}^{'}] - \sinh(\alpha^{'}Y_1)[\alpha^{'}kE_5^{'} + \alpha^{'}E_{11}^{'}] - Y_1[2kE_6^{'} + 2E_6^{'}]]$ (B11i)

It follows that Eq. (B6a), (B6b) and Eq. (B8) are identical to the nanofluid and porous solid and thick-walls thermal equations in Ting et al. [11] and Hunt et al. [14] with the heat generation by viscous dissipation equal to 0.

References

[1] Thomas Wirth, Microreactors in Organic Chemistry and Catalysis, John Wiley & Sons, 2013.
[2] Gunther Kolb, Microstructured reactors for distributed and renewable production of fuels and electrical energy, Chem. Eng. Process. Process. Intensif. 65 (2013) 1–44.
[3] Gunther Kolb, Volker Hessel, Micro-structured reactors for gas phase reactions, Chem. Eng. J. 98 (1-2) (2004) 1–38.
[4] Helmut Pennemann, Gunther Kolb, Microstructured reactors as efficient tool for the operation of selective oxidation reactions, Catal. Today 278 (2016) 3–21.
[5] Manuel Götz, Jonathan Lefebvre, Friedemann Mörs, Amy Mc Daniel Koch, Frank Graf, Siegfried Bajohr, Rainer Reimert, Thomas Kolb, Renewable Power-to-Gas: a technological and economic review, Renew. Energy 85 (2016) 1371–1390.
[6] Norbert Kockmann, Transport Phenomena in Micro Process Engineering, Springer Science & Business Media, 2007.
[7] Niket S. Kaisare, Dionisios G. Vlachos, A review on microcombustion: Fundamentals, devices and applications, Prog. Energy Combust. Sci. 38 (3) (2012) 321–359.
[8] Ran Sui, Nikolaos I. Prasianakis, John Mantzaras, Nithin Mallya, Jürgen Theile, Damien Lagrange, Martin Friess, An experimental and numerical investigation of the combustion and heat transfer characteristics of hydrogen-fueled catalytic microreactors, Chem. Eng. Sci. 141 (2016) 214–230.
[9] Michael J. Stutz, Dimos Poulikakos, Effects of microreactor wall heat conduction on the reforming process of methane, Chem. Eng. Sci. 60 (24) (2005) 6983–6997.
[10] Tiew Wei Ting, Yew Mun Hung, Ningqun Guo, Entropy generation of viscous dissipative nanofluid flow in thermal non-equilibrium porous media embedded in microchannels, Int. J. Heat Mass Transf. 81 (2015) 862–877.
[11] Tiew Wei Ting, Yew Mun Hung, Ningqun Guo, Entropy generation of viscous dissipative nanofluid convection in asymmetrically heated porous microchannels with solid-phase heat generation, Energy Convers. Manage. 105 (2015) 731–745.
[12] Takashi Kamijo, Yuji Suzuki, Nobuhide Kasagi, Takashi Okamasa, High-temperature micro catalytic combustor with Pd/nano-porous alumina, Proc. Combust. Inst. 32 (2) (2009) 3019–3026.
[13] Taegyu Kim, Sejin Kwon, Design, fabrication and testing of a catalytic microreactor for hydrogen production, J. Micromechan. Microeng. 16 (9) (2006) 1760–1768.
[14] Graeme Hunt, Nader Karimi, Bijan Yadollahi, Mohsen Torabi, The effects of exothermic catalytic reactions upon combined transport of heat and mass in porous microreactors, Int. J. Heat Mass Transf. 134 (2019) 1227–1249.
[15] S. Thiyagarajan, V. Edwin Geo, B. Ashok, K. Nanthagopal, R. Vallinayagam, C.G. Saravanan, P. Kumaran, NO x emission reduction using permanent/electromagnet-based fuel reforming system in a compression ignition engine fueled with pine oil, Clean Technol. Environ. Policy (2019) 1–11.
[16] S. Thiyagarajan, Ankit Sonthalia, V. Edwin Geo, B. Ashok, K. Nanthagopal, V. Karthickeyan, B. Dhinesh, Effect of electromagnet-based fuel-reforming system on high-viscous and low-viscous biofuel fueled in heavy-duty CI engine, J. Therm. Anal. Calorim. (2019) 1–12.
[17] Avinash Kumar Agarwal, Jai Gopal Gupta, Atul Dhar, Potential and challenges for large-scale application of biodiesel in automotive sector, Prog. Energy Combust. Sci. 61 (2017) 113–149.
[18] Sirapassorn Kiatphuengporn, Pongsakorn Jantaratana, Jumras Limtrakul, Metta Chareonpanich, Magnetic field-enhanced catalytic CO2 hydrogenation and selective conversion to light hydrocarbons over Fe/MCM-41 catalysts, Chem. Eng. J. 306 (2016) 866–875.
[19] Chuleehat Sriakkarin, Wasakon Umchoo, Waleeporn Donphai, Yingyot Poo-arporn, Metta Chareonpanich, Sustainable production of methanol from CO2 over 10Cu-10Fe/ZSM-5 catalyst in a magnetic field-assisted packed bed reactor, Catal. Today 314 (2018) 114–121.
[20] A.K. Hakeem, P. Abdul, N. Renuka, Vishnu Ganesh, R. Kalaivanan, B. Ganga, Influence of inclined Lorentz forces on boundary layer flow of Casson fluid over an impermeable stretching sheet with heat transfer, J. Magn. Magn. Mater. 401 (2016) 354–361.
[21] Nader Karimi, Daniel Agbo, Ammar Talat Khan, Paul L. Younger, On the effects of exothermicity and endothermicity upon the temperature fields in a partially-filled porous channel, Int. J. Therm. Sci. 96 (2015) 128–148.
[22] Mohsen Torabi, Nader Karimi, Kaili Zhang, G.P. Peterson, Generation of entropy and forced convection of heat in a conduit partially filled with porous media–local thermal non-equilibrium and exothermicity effects, Appl. Therm. Eng. 106 (2016) 518–536.
[23] Graeme Hunt, Mohsen Torabi, Lilian Govone, Nader Karimi, Amirfarhang Mehdizadeh, Two-dimensional heat and mass transfer and thermodynamic analyses of porous microreactors with Soret and thermal radiation effects—an analytical approach, Chemical Engineering and Processing-Process Intensification 126 (2018) 190–205.
[24] T. Hayat, S.A. Shehzad, A. Alsaedi, Soret and Dufour effects on magnetohydrodynamic (MHD) flow of Casson fluid, Appl. Math. Mech. 33 (10) (2012) 1301–1312.
[25] David G.P. Guthrie, Mohsen Torabi, Nader Karimi, Combined heat and mass transfer analyses in catalytic microreactors partially filled with porous material-The influences of nanofluid and different porous-fluid interface models, Int. J. Therm. Sci. 140 (2019) 96–113.
[26] Rei-Yu Chein, Li-Chang Chen, Yen-Cho Chen, J.N. Chung, Heat transfer effects on the methanol-steam reforming with partially filled catalyst layers, Int. J. Hydrogen Energy 34 (13) (2009) 5398–5408.
[27] Rei-Yu Chein, Yen-Cho Chen, J.N. Chung, Thermal resistance effect on methanol-steam reforming performance in micro-scale reformers, Int. J. Hydrogen Energy 37 (1) (2012) 250–262.
[28] Donald A. Nield, Adrian Bejan, Convection in Porous media vol. 3, springer, New York, 2013.
[29] Kambiz Vafai, Handbook of Porous Media, CRC Press, 2015.
[30] Rei-Yu Chein, Yen-Cho Chen, J.N. Chung, Thermal resistance effect on methanol-steam reforming performance in micro-scale reformers, Int. J. Hydrogen Energy 37 (1) (2012) 250–262.
[31] Dae-Young Lee, Kambiz Vafai, Analytical characterization and conceptual assessment of solid and fluid temperature differentials in porous media, Int. J. Heat Mass Transf. 42 (3) (1999) 423–435.
[32] Guillermo Ibáñez, Aracely López, Joel Pantoja, Joel Moreira, Juan A. Reyes, Optimum slip flow based on the minimization of entropy generation in parallel plate microchannels, Energy 50 (2013) 143–149.
[33] Yasser Mahmoudi, Nader Karimi, Numerical investigation of heat transfer enhancement in a pipe partially filled with a porous material under local thermal non-equilibrium condition, Int. J. Heat Mass Transf. 68 (2014) 161–173.
[34] Mohsen Torabi, Nader Karimi, Khaili Zhang, Heat transfer and second law analyses of forced convection in a channel partially filled by porous media and featuring internal heat sources, Energy 93 (2015) 106–127.
[35] Craig Dickson, Mohsen Torabi, Nader Karimi, First and second law analysis of nanofluid convection through a porous channel-The effects of partial filling and internal heat sources", Appl. Therm. Eng. 103 (2016) 459–480.
[36] Naramgari Sandeep, Olubode Kolade Koriko, and Isaac Lare Animasaun. "modified kinematic viscosity model for 3D-Casson fluid flow within boundary layer formed

on a surface at absolute zero, J. Mol. Liq. 221 (2016) 1197–1206.
[37] Muhammad Ijaz Khan, Muhammad Waqas, Tasawar Hayat, Ahmed Alsaedi, A comparative study of Casson fluid with homogeneous-heterogeneous reactions, J. Colloid Interface Sci. 498 (2017) 85–90.
[38] Violeta Paunovic, Vitaly Ordomsky, Maria Fernanda Neira D'Angelo, Jaap C. Schouten, T. Alexander Nijhuis, Catalyst coating on prefabricated capillary microchannels for the direct synthesis of hydrogen peroxide, Ind. Eng. Chem. Res. 54 (11) (2015) 2919–2929.
[39] Evgeny V. Rebrov, Angel Berenguer-Murcia, Helen E. Skelton, Brian F.G. Johnson, Andrew E.H. Wheatley, Jaap C. Schouten, Capillary microreactors wall-coated with mesoporous titania thin film catalyst supports, Lab Chip 9 (4) (2009) 503–506.
[40] Su Cheun Oh, Emily Schulman, Junyan Zhang, Jiufeng Fan, Ying Pan, Jianqiang Meng, Dongxia Liu, Direct non-oxidative methane conversion in a millisecond catalytic wall reactor, Angew. Chemie 131 (2019) 7157–7160.
[41] John Mantzaras, Understanding and modeling of thermofluidic processes in catalytic combustion, Catal. Today 117 (4) (2006) 394–406.
[42] Mohammad Hossein Abolbashari, Navid Freidoonimehr, Foad Nazari, Mohammad Mehdi Rashidi, Analytical modeling of entropy generation for Casson nano-fluid flow induced by a stretching surface, Adv. Powder Technol. 26 (2) (2015) 542–552.
[43] H.J. Xu, C.Y. Zhao, Z.G. Xu, Analytical considerations of slip flow and heat transfer through microfoams in mini/microchannels with asymmetric wall heat fluxes, Appl. Therm. Eng. 93 (2016) 15–26.
[44] Graeme Hunt, Nader Karimi, Mohsen Torabi, Two-dimensional analytical investigation of coupled heat and mass transfer and entropy generation in a porous, catalytic microreactor, Int. J. Heat Mass Transf. 119 (2018) 372–391.
[45] T. Hayat, M. Waqas, S.A. Shehzad, A. Alsaedi, A model of solar radiation and Joule heating in magnetohydrodynamic (MHD) convective flow of thixotropic nanofluid, J. Mol. Liq. 215 (2016) 704–710.
[46] Chaoli Zhang, Liancun Zheng, Xinxin Zhang, Goong Chen, MHD flow and radiation heat transfer of nanofluids in porous media with variable surface heat flux and chemical reaction, Appl. Math. Model. 39 (1) (2015) 165–181.
[47] Michael F. Modest, Radiative Heat Transfer, Academic press, 2013.
[48] William M. Deen, Analysis of Transport Phenomena, Topic in Chemical Engineering, Oxford University Press, New York, 1998.
[49] Chaoli Zhang, Liancun Zheng, Xinxin Zhang, Goong Chen, MHD flow and radiation heat transfer of nanofluids in porous media with variable surface heat flux and chemical reaction, Appl. Math. Model. 39 (1) (2015) 165–181.
[50] Theodore L. Bergman, Frank P. Incropera, Adrienne S. Lavine, David P. DeWitt, Fundamentals of Heat and Mass Transfer, John Wiley & Sons, 2011.
[51] G.H.R. Kefayati, Simulation of double diffusive natural convection and entropy generation of power-law fluids in an inclined porous cavity with Soret and Dufour effects (Part II: entropy generation), Int. J. Heat Mass Transf. 94 (2016) 582–624.
[52] Mohsen Torabi, Nader Karimi, G.P. Peterson, Shannon Yee. "Challenges and progress on the modelling of entropy generation in porous media: a review, Int. J. Heat Mass Transf. 114 (2017) 31–46.
[53] Yi Shen Chee, Tiew Wei Ting, Yew Mun Hung, Entropy generation of viscous dissipative flow in thermal non-equilibrium porous media with thermal asymmetries, Energy 89 (2015) 382–401.
[54] Meisam Habibi Matin, Ioan Pop, Forced convection heat and mass transfer flow of a nanofluid through a porous channel with a first order chemical reaction on the wall, Int. Commun. Heat Mass Transf. 46 (2013) 134–141.